

Water Resources Research®



RESEARCH ARTICLE

10.1029/2025WR040706

Key Points:

- Water dynamics and land cover heterogeneity along hillslope are explicitly considered in the land surface model MATSIRO
- It reveals more soil water in valleys and greater (less) evapotranspiration (runoff) on densely vegetated parts of hillslope
- The appropriate resolution of hillslope vegetation in land surface model widely modulates and better captures the water and energy budgets

Supporting Information:

Supporting Information may be found in the online version of this article.

Correspondence to:






S. Li,
shuping@iis.u-tokyo.ac.jp

Citation:

Li, S., Yamazaki, D., Tozawa, T., Adachi, K., Nitta, T., Zhao, G., et al. (2025). Resolving land cover heterogeneity along hillslope improves simulation of terrestrial water and energy budgets. *Water Resources Research*, 61, e2025WR040706. <https://doi.org/10.1029/2025WR040706>

Received 3 APR 2025
Accepted 29 AUG 2025

Resolving Land Cover Heterogeneity Along Hillslope Improves Simulation of Terrestrial Water and Energy Budgets

Shuping Li¹ , Dai Yamazaki¹ , Tomohiro Tozawa¹, Kota Adachi¹, Tomoko Nitta², Gang Zhao³ , Xudong Zhou⁴ , and Kei Yoshimura¹ 

¹Institute of Industrial Science, The University of Tokyo, Tokyo, Japan, ²Faculty of Science and Engineering, Chuo University, Tokyo, Japan, ³Department of Transdisciplinary Science and Engineering, Institute of Science Tokyo, Tokyo, Japan, ⁴Institute of Hydraulic and Ocean Engineering, Ningbo University, Ningbo, China

Abstract Horizontal water transport from hills to valleys widely dictates vegetation growth and modulates terrestrial water and energy budgets. However, land cover on hillslopes remains oversimplified in many current land surface models (LSMs) despite its critical role in controlling terrestrial water and energy fluxes. To this end, we focused on Africa to investigate how explicit representation of hillslope water dynamics and land cover conditions in LSM influences terrestrial water and energy budgets. A sub-grid catchment-based strategy was implemented in the LSM MATSIRO, in which the hillslope water dynamics and land cover heterogeneity were modeled in discretized height bands of representative hillslopes. Through several experiments that differed in terms of complexity in representing water and vegetation heterogeneity along hillslope, the impact of representing them in LSM is evaluated and validated. Increasingly accurate representation of the heterogeneities amplified the variabilities of the simulated water and energy budgets, particularly in equatorial Africa. The hill-to-valley water dynamics aside, more realistic representation of the hillslope vegetation distribution aligned with known differences in soil water content (e.g., denser vegetation exists along riversides in arid regions). Such representations changed the soil water contents, runoffs, and evapotranspiration of almost 5%, 7% and 18% of the total African land areas studied, respectively. By better capturing hillslope-scale rainfall interception and transpiration with the improved model, the results are more consistent with observed discharges and leaf area index. Overall, an LSM that considers hillslope water dynamics and land cover heterogeneity substantially modulates and better captures the terrestrial water and energy budgets.

Plain Language Summary Accurate representation of hillslope water dynamics by a land surface model is important when seeking to describe water and energy conditions precisely at fine space scales. That being said, the complex land surface conditions (e.g., the land cover type) that directly affect these dynamics and therefore influence the water and energy status of land are treated in a simple manner and yet to be thoroughly addressed. In this study, we included hillslope heterogeneity in a LSM and assessed the impact thereof on terrestrial water and energy budgets across the African continent. The results show that, hillslope water dynamics aside, more realistic representations of hillslope vegetation distribution that roughly matched differences in soil water contents (e.g., denser vegetation along riversides in arid regions) revealed several distinct forms of soil water movement and evapotranspiration over the African continent. Compared to observational data, the results of modeling that considered the complex land surface conditions were more accurate. We emphasize the need to resolve hillslope water dynamics and land cover heterogeneity explicitly if a LSM is to be appropriate.

1. Introduction

Over the last six decades, remarkable advances have been made in the development of land surface models (LSMs) that simulate surface processes and the influences of weather and climate (Stephens et al., 2023). Manabe (1969) was the first to propose a bucket model that calculated the feedback of latent and sensible heat fluxes to the atmosphere. Since then, LSMs have gradually evolved to represent more complex land processes. Topographic parameters were introduced to allow calculation of the terrestrial water surplus (runoff) that constituted the surface water network (Milly et al., 2014; Ngo-Duc et al., 2007). Later, grid cells were used to represent the land-atmosphere flux exchanges over vegetation canopies and bare ground, facilitating representation of water transpiration by the canopy layer (Dickinson, 1984). However, even at the highest resolution

© 2025. The Author(s).

This is an open access article under the terms of the [Creative Commons Attribution-NonCommercial-NoDerivs License](#), which permits use and distribution in any medium, provided the original work is properly cited, the use is non-commercial and no modifications or adaptations are made.

(25 km) of modern climate models, land surface processes that span the various subdisciplines of biophysics and hydrology can yield markedly different results for even a single climatic grid cell (Adachi et al., 2024; Fox et al., 2008; Lundquist & Dettinger, 2005; Tai et al., 2017). As new data became available and computational capacity increased, treatment of sub-grid heterogeneity by LSMs advanced remarkably (Chaney et al., 2018; Lawrence et al., 2019; Subin et al., 2014; Swenson et al., 2019; Wood et al., 2011). The spatial resolutions of LSMs and associated atmospheric models are becoming increasingly refined. To allow simulations across multiple land scales, most modern LSMs, such as MATSIRO (Takata et al., 2003), JULES (Burton et al., 2019), CLM5 (Lawrence et al., 2019) and ORCHIDEE (Naudts et al., 2015) use a sub-grid tiling scheme. Within a grid cell, tiles are typically defined as spatially implicit aggregations of the areas affiliated with particular land surface categories.

Although such efforts address the complexity of land surface processes to some extent, integration of LSMs using new theories that better describe how land processes are governed has been slow (Byrne et al., 2024). Specifically, current models of land surface complexity consider only vertical water exchange (to and from the atmosphere); connections between neighboring land tiles are neglected. This does not close the gap between model resolution and the spatial resolution at which certain key processes occur (Li et al., 2024; Swenson et al., 2019). For example, hillslope water dynamics are greatly influenced by (often complex) local topographic conditions that are under-represented in large-scale models, and it remains unclear how horizontal water fluxes affect land-surface and near-surface processes (Simpson et al., 2024). Valleys tend to be wetter than ridges because water flows downhill. In most cases, the resulting subsurface water gradient enhances vegetation growth on both the lower slopes of dry catchments and the upper slopes of wet catchments owing to water stress and oxygen stress, respectively (Fan et al., 2019; Li et al., 2024). In this context, modern LSMs seek not simply to represent land surface heterogeneity, but rather to offer good resolution of both hillslope water dynamics and the variability in hillslope vegetation distribution. This has posed some challenges in attempts to resolve the extensive terrestrial water and energy fluxes that occur at sub-grid scales better (Chaney et al., 2018). Despite the importance of the topic, many large-scale LSMs do not yet reflect hydrological processes optimally (Bierkens, 2015; Brooks et al., 2015; Clark et al., 2015; Fan et al., 2019).

Given such concerns, many efforts have been made to enhance LSM hydrological process representations, and several land models have been used to study water cycle changes at the catchment, continental, and global scales (Clark et al., 2015). To capture horizontal water dynamics, some suggested segmenting terrestrial areas by hydrological response units along hillslopes (Fan et al., 2019; Swenson et al., 2019). Such schemes define hydrological response units as fractions of a grid cell, therefore representing the physical horizontal water flow without dramatically elevating the computational costs. Based on this concept, LSM developers have recently improved the hydrological processes of several models (Ajami et al., 2016; Chaney et al., 2018; Subin et al., 2014; Swenson et al., 2019). For example, Subin et al. (2014) reported how the sub-grid hillslope hydrology of the GFDL model could be better resolved, and noted that improved representation of saturated lowland areas increased the soil carbon budget. Using high-resolution environmental data, Chaney et al. (2018) introduced a hierarchical, multivariate clustering approach into the LM4-HB model. This disaggregated hydrologically interconnected tiles and ensured high-level modeling efficiency. Swenson et al. (2019) implemented representative hillslopes into the CLM, and found that the impact of hydrological tiling was strongest in semi-arid areas. Despite these efforts, we do not yet fully grasp the importance of consistently resolving the water dynamics and land cover heterogeneity along hillslopes. It remains unclear whether it is appropriate to consider that sub-grid vegetation distribution corresponds to the hill-to-valley water gradient. We suggest that accurate representation of how vegetation modifies precipitation, soil water transpiration, and evaporation would improve model predictions of terrestrial water and energy budgets.

In this study, when incorporating the water dynamics and land cover heterogeneity along hillslopes into an LSM, we employed a previously proposed catchment-based strategy (Li et al., 2024) that considers horizontal water flow. The modeling units are representative hillslopes divided into hydrologically connected height bands. These were implemented in the LSM MATSIRO using an Integrated Land Simulator (ILS, Nitta et al., 2020; the details are in Section 2). The boundary conditions of the hillslope topography and land cover were objectively extracted from high-resolution data currently available at both continental and global scales. In a variety of experiments, we use the African continent as our test bed and discuss the significance of consistent LSM-mediated representation of hillslope water dynamics and land cover heterogeneity when evaluating terrestrial water and energy budgets.

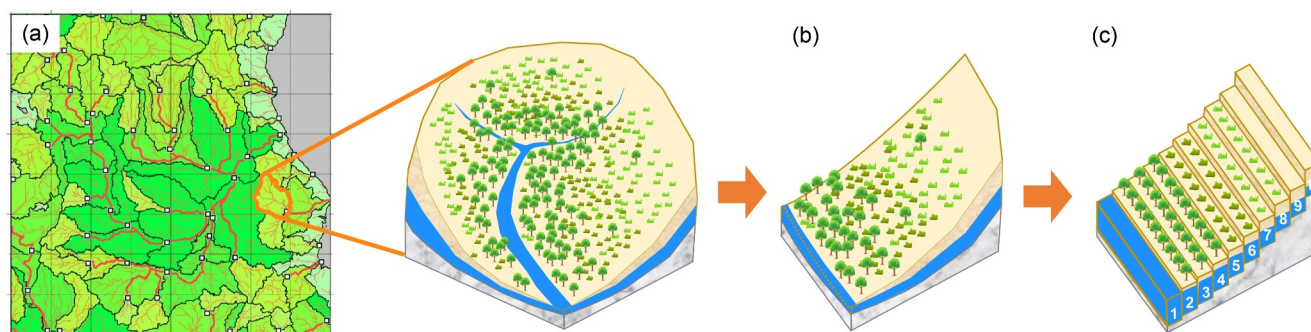


Figure 1. A schematic of the catchment-based strategy. (a) A terrestrial area is segmented into unit catchments of similar sizes; (b) a representative hillslope is used to conceptually approximate the unit catchment; and (c) that hillslope is vertically discretized into 10 height bands, each of the same surface area.

2. Models

This section overviews the previously developed land models. First, the LSM MATSIRO is described. Then, the global hydrodynamic model CaMa-Flood is introduced. Using the ILS framework, MATSIRO was de-coupled from the parent general circulation model (GCM) and offline simulations were then conducted using CaMa-Flood.

2.1. Land Surface Model: MATSIRO

The process-based physical model MATSIRO (Takata et al., 2003), as the land component of the GCM termed Model for Interdisciplinary Research on Climate (MIROC, Hasumi & Emori, 2004), was utilized in the present study.

MATSIRO simulates water and energy status and their physical exchange between the land surface and the atmosphere, with consideration of soil moisture (SM, the volumetric water content), runoff, the latent heat flux (Q_{le}), the sensible heat flux (Q_h), the water table depth, and other variables. In MATSIRO, the canopy is a single layer, the albedo and bulk coefficients of which are evaluated using a multilayer canopy model. Interception of evaporation by the canopy, and transpiration, are estimated using photosynthetic parameters of the Farquhar type (Farquhar et al., 1980) and the SiB2 values (Sellers et al., 1986, 1996). Energy fluxes are calculated at the surfaces of the ground and canopy in snow-free and -covered portions of each grid cell. The snow layers are dynamic, increasing (if necessary) to a maximum of three depending on the snow water equivalent. The soil column is divided into six discrete layers at depth boundaries 5, 20, 75, 100, 200, and 1,000 cm from the surface and the soil temperature, SM, and frozen SM calculated for each layer. A simplified TOPMODEL (Beven & Kirkby, 1979; Stieglitz et al., 1997) simulates runoff generation and estimate surface and subsurface runoff separately.

2.1.1. Horizontal Water Flow

MATSIRO can simulate horizontal water dynamics by implementing a catchment-based strategy (Adachi et al., 2024; Li et al., 2024; Tozawa et al., 2019). Based on the high-resolution hydrographic data set termed MERIT Hydro, the flow directions of pixels are merged to create a terrestrial boundary map of the unit catchments using the upscaling method termed Flexible Location of Waterways (FLOW, Yamazaki et al., 2009). FLOW employs a uniform catchment size when exploring river channel connectivity, and then allocates outlets to all river networks defined as the main river channels of the unit catchments. As a result, each rectangular grid unit becomes spatially paired with a unit catchment of similar size (Figure 1a). A typical catchment generally includes many complex hillslopes, among which the land cover transitions from channels to ridgelines are assumed to be very similar. To ensure both conceptual clarity and computational efficiency, these complex hillslopes are then theoretically collapsed into a concise representative hillslope based on the relative hillslope heights above the main river channel (Figure 1b). Each representative hillslope is then discretized into 10 vertical height bands to enable consideration of horizontal water flow. As hillslope water converges to the nearest stream rather than to the lowest point of the catchment, the soil wetness generally aligns with the distance to the nearest stream. Thus, during height band discretization, the elevation relative to the nearest stream point, not the absolute elevation, is used. To discretize the height bands evenly, the areas of all bands are the same (Figure 1c).

The horizontal water flux q between neighboring height bands is given by Darcy's law:

$$q = -\frac{K_O}{f} I e^{(-f\bar{z})} \quad (1)$$

$$I = \frac{(\bar{h}_{i+1} - \bar{z}_{i+1}) - (\bar{h}_i - \bar{z}_i)}{d_i} \quad (2)$$

where K_O is the saturation hydraulic conductivity at the ground surface, f denotes the reduction constant, I is the hydraulic gradient between two neighboring bands, and \bar{z} denotes the mean water table depth. \bar{h}_i and \bar{z}_i are the mean relative height above the main river channel and the mean water table depth at height band i , respectively. d_i denotes the horizontal distance between height band i and height band $i + 1$. Note that the horizontal water flux q is considered only when the water table is above the frozen soil layer. The q simulation may affect the status of source term S_w via:

$$S_w = -F_{\text{root}} - R_O - q \quad (3)$$

where F_{root} denotes the root water uptake and R_O is the total runoff. Then, the vertical SM movement is solved using Richards' equation:

$$\rho_w \frac{w_{(k)}^{\tau+1} - w_{(k)}^{\tau}}{\Delta t_L} = \frac{F_{w(k+\frac{1}{2})} - F_{w(k-\frac{1}{2})}}{\Delta z_{g(k)}} + S_{w(k)} \quad (k = 1, \dots, K_g) \quad (4)$$

where ρ_w denotes the density of water, $w_{(k)}^{\tau+1} - w_{(k)}^{\tau}$ is the change in SM content of the k th layer at time step τ , Δt_L denotes the time step length, $F_{w(k+\frac{1}{2})} - F_{w(k-\frac{1}{2})}$ is the SM flux at the k th soil layer, $\Delta z_{g(k)}$ denotes the thickness of the k th soil layer, $S_{w(k)}$ is the source term of the k th soil layer, and K_g is 6. Then the SM status within any height band is updated using the LU factorization method as follows:

$$w_{(k)}^{\tau+1} = w_{(k)}^{\tau} + \Delta w_{(k)} \quad (5)$$

As w is updated for each height band, both \bar{z} and the fraction of the saturated area A_{sat} change. This affects the subsurface runoff R_{O_b} , the saturation excess runoff R_{O_s} , the infiltration excess runoff R_{O_i} , and the total runoff R_O :

$$R_{O_b} = \frac{K_O \tan \beta_s}{f L_s} e^{(1-f\bar{z})} \quad (6)$$

$$R_{O_s} = (Pr_c^{**} + Pr_l^{**}) A_{\text{sat}} \quad (7)$$

$$R_{O_i} = A_c Ro_i^c + (1 - A_c) Ro_i^{\text{nc}} \quad (8)$$

$$Ro_i^c = \max(Pr_l^{**} - K_{s(1)}, 0) (1 - A_{\text{sat}}) \quad (9)$$

$$Ro_i^{\text{nc}} = \max\left(\frac{Pr_c^{**}}{A_c} + Pr_l^{**} - K_{s(1)}, 0\right) (1 - A_{\text{sat}}) \quad (10)$$

$$R_O = R_{O_b} + R_{O_s} + R_{O_i} + R_{O_o} \quad (11)$$

where Pr_c^{**} denotes the convective rainfall intensity; Pr_l^{**} is the non-convective rainfall intensity attributable to rain interception by the canopy; A_c denotes the fraction of the precipitation area; Ro_i^c and Ro_i^{nc} are the R_{O_i} for the convective and non-convective precipitation areas, respectively; $K_{s(1)}$ denotes the saturation hydraulic conductivity in the uppermost soil layer; and R_{O_o} is the overflow runoff.

2.1.2. Land Cover

MATSIRO tiles the land surface to represent sub-grid land surface types. This mimics the heterogeneous land surface processes at higher resolutions only partially (MATSIRO6 Document Writing Team, 2021). Basically, a single land surface grid can be both implicitly and flexibly divided into different numbers of tiles. Three sub-grid tiles—lake, potential vegetation and cropland—serve as MATSIRO defaults to control the computational cost. The vegetation types of the Simple Biosphere Model 2 scheme (Sellers et al., 1986, 1996) fall into 10 categories including continental ice (Table S1 in Supporting Information S1). The average fluxes at a land surface F are:

$$F = F_{\text{lake}} f_{\text{lake}} + \sum_{i=1}^n F_i f_i \quad (12)$$

$$f_i = f_i'' (1 - f_{\text{lake}}) \quad (13)$$

$$\sum_{i=1}^n f_i'' = 1 \quad (14)$$

where F_{lake} denotes fluxes at a lake surface, f_{lake} is the fractional weight of lakes, F_i denotes the fluxes at a land surface of land cover type i , f_i is the fractional weight of land cover type i (the sum of f_{lake} and f_i always equals 1), and f_i'' denotes the sub-fractional weights of land cover type i excluding the lake fraction.

2.2. Global Hydrodynamic Model: CaMa-Flood

CaMa-Flood is a physical, distributed, global, river routing model (Yamazaki et al., 2011). The model uses a local inertial equation that is a simplified form of the one-dimensional Saint-Venant equation (Bates et al., 2010; Yamazaki et al., 2013). The advection term is neglected to allow computationally efficient simulations of continental-scale river hydrodynamics.

By routing the runoff generated by the LSM to a pre-derived river network map, CaMa-Flood simulates the hydrodynamics over both rivers and floodplains in 10-min time steps. The model simulates river discharge, water surface elevation, water surface area, and surface water storage. CaMa-Flood uses catchments of similar size to the LSM grid cell (the details are in Li et al., 2024). CaMa-Flood considers channel length, channel width, channel depth (bank height), surface altitude, Manning's coefficient, and unit catchment area as parameters.

2.3. Integrated Land Simulator

The Integrated Land Simulator (ILS) framework was recently developed to improve the land surface component of the Model for Interdisciplinary Research on Climate (MIROC) (Nitta et al., 2020). The ILS contains two land models, MATSIRO and CaMa-Flood. An I/O component that inputs and outputs files serves as an independent executable. Based on a general-purpose coupler termed Jcup, multiple terrestrial models are linked (Arakawa et al., 2020). Currently, MATSIRO is one-way coupled with CaMa-Flood within ILS. Runoffs generated by MATSIRO are input to CaMa-Flood (via Jcup) to simulate hydrodynamic processes.

The pixels of the flow directions derived using a high-resolution hydrographic data set are merged by the FLOW upscaling method to create terrestrial boundary maps of unit catchments (Yamazaki et al., 2009). CaMa-Flood catchments are irregular in shape, but the grid units of typical LSMs such as MATSIRO are regular in shape. To improve hydrological process representation, MATSIRO treats the unit catchment as a pseudo-modeling unit when coupling models of disparate grid coordinates. This facilitates data exchange within the ILS by establishing a one-to-one interpolation wherein each unit catchment in CaMa-Flood is spatially paired with a catchment in MATSIRO. Then, an LSM catchment-based strategy can simulate horizontal hydrological processes using the discretized height bands.

3. Experimental Setting

3.1. Representation of Water Dynamics and Land Cover Heterogeneity Along Hillslopes in LSM

We performed four experiments to test the significance of explicitly representing the water dynamics and land cover heterogeneity along hillslope in LSM (Figure 2 and Table 1).

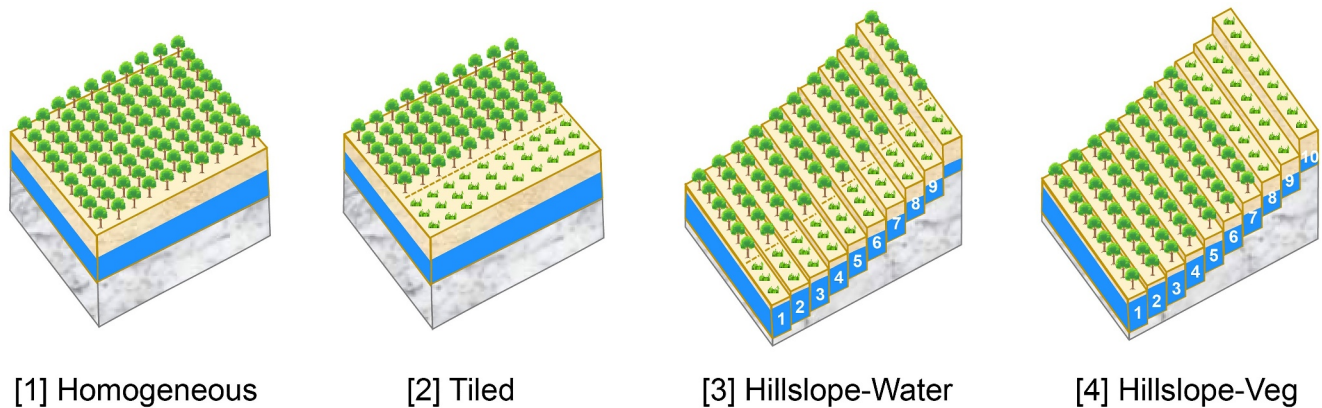


Figure 2. A schematic of the four experimental settings. The brown dashed lines between the different land cover tiles of experimental settings [2] and [3] indicate separate simulations of the land surface processes in different tiles.

In experiment [1], land surface processes (water and energy fluxes) occurred only vertically and the terrestrial boundary conditions such as the land cover type were homogeneous across the catchment. Specifically, the dominant land cover type was identified by reference to the high-resolution land cover map and represented the only form of catchment land cover. The average high-resolution leaf area index (LAI) corresponding to the dominant land cover type served as the vegetation parameter.

Experiment [2] differed from [1] in terms of land cover heterogeneity representation. The tiling scheme widely used by modern LSMs was employed. The two major land cover types that occupied the largest and second largest proportions of the catchment area were identified. To ensure concise representation, the land cover conditions of the catchment were exclusively and implicitly represented by the two identified types, whose proportions over the catchment area summed to 1. Then, the high-resolution LAIs of the two types were averaged and treated as the vegetation parameters. The simulations from the two land cover types were averaged by the area weights to present an overall result for the catchment synthetically.

In experiment [3], the catchment-based strategy is employed to represent the hillslope heterogeneity in land surface modeling (Li et al., 2024). Based on elevations relative to the nearest streams, the entire catchment was evenly discretized into 10 height bands with the same area. Each band served as an independent unit when modeling the vertical energy and water fluxes. By Darcy's law, subsurface water may flow between neighboring bands if permitted by the subsurface hydraulic gradient. This affects the amount of subsurface water within each modeling unit. Beginning with this experiment, the water dynamics were simulated in two dimensions (vertical and horizontal). The height bands did not differ in terms of land cover, but the heterogeneity within each height band was addressed by the tiling. As in experiment [2], in each band the land cover boundary was implicitly represented by the two major land cover types identified at the catchment level. The average LAIs corresponding to the two types were calculated and treated as homogeneous vegetation parameters for all height bands. The weighted average of the simulation results derived using the two types represented the overall results for each height band.

Experiment [4] was similar to experiment [3] in terms of the representation of the hillslope water dynamics. However, the representation of the land cover heterogeneity differed. The land cover of each height band was the dominant land cover type in that band. It indicates a disparate strategy in representing land cover heterogeneity in contrast to experiment [3]. Although the land cover representations of the height bands are affected by several forms of bias, these were assumed to be minor in hillslope-/climate-dominated landscapes where the vertical land cover evolution is consistent with the wetness or climatic gradient. Accordingly, the high-resolution LAI corresponding to the dominant land cover type of each band was averaged and served as the vegetation parameter.

A comparison of the results of experiments [1] and [2] revealed how well land cover heterogeneity was reflected by the tiling scheme. Specifically, both F_i

Table 1
Information on the Four Experimental Settings of Figure 2

Experiment	Water dynamics	Land cover
[1] Homogeneous	Vertical	Homogeneous
[2] Tiled	Vertical	Heterogeneous (TS ^a)
[3] Hillslope-Water	Vertical and Horizontal	Heterogeneous (TS ^a)
[4] Hillslope-Veg	Vertical and Horizontal	Heterogeneous (CBS ^a)

^aTS and CBS: Tile scheme and catchment-based strategy, respectively.

and f_i in Equations 12–14 changed. A comparison of the results of experiments [3] and [4] allowed further evaluation of how two different representations of land cover heterogeneity impacted land surface processes. Unlike a conventional tiling scheme, our catchment-based strategy considers sub-grid land cover heterogeneity by assigning a unique land cover type to each band. This scheme can then become as efficient as a tiling scheme but better reveals the impacts of hillslope land cover heterogeneity.

3.2. Validating the Modeling Results

A straightforward method of model validation is a comparison of point-based observation data with the simulations using a diagnostic metric (Wood et al., 2011). Such direct validation of SM, Qle, and Qh against the observations from ISMN and FLUXNET is discussed in Text S1 in Supporting Information S1. However, given the scaling error inherent between point-based observations and the areal-based modeling results for SM, Qle, and Qh, local environmental conditions near gauge stations may be underrepresented by the model, possibly inducing large biases during validation. It leads to the concern that direct observation from FLUXNET and ISMN might not be appropriate for validating LSM results.

Given this concern, we simply compared discharges observed at GRDC stations to those simulated by CaMa-Flood (running the ILS framework) in each catchment. The Nash–Sutcliffe efficiency (NSE; Nash & Sutcliffe, 1970) was used to evaluate the goodness of fit:

$$NSE = 1 - \frac{\sum_{i=1}^N (O_i - S_i)^2}{\sum_{i=1}^N (O_i - \bar{O})^2} \quad (15)$$

where O_i and S_i denote the observed and modeled values at time i , respectively. \bar{O} is the mean observational value. $NSE = 1$ indicates a perfect correspondence between simulation and observation, $NSE = 0$ indicates that the simulation is as good as the observation mean, and $NSE < 0$ indicates that the simulation is a worse predictor than the mean observational value. GRDC stations for which the simulated ($NSE < -1$) were excluded from the validation analysis.

3.3. Study Region

The ILS ran over the African continent ranging from 38°N to 36°S latitude and 19°W to 52°E longitude (Figure 3a). This test bed was selected for the following reasons.

1. A previous study revealed many hillslope- and climate-dominated landscapes across the continent (Li et al., 2024), implying a need to resolve sub-grid hillslope heterogeneity. For example, the LAI gradient (a proxy of vegetation growth) from the lower to the higher height bands calculated via linear regression is shown in Figure 3b.
2. The continent is characterized by a mix of climatic and topographic conditions, aiding examination of the hillslope water dynamics under different environmental conditions.
3. The natural environment is not greatly perturbed by human activity (urban and agricultural areas), aiding the analysis of hillslope water dynamics.

A regional mapping table was created using the tool termed Spheroidal Coordinates Regridding Interpolation Table Generator (SPRING, Takeshima & Yoshimura, 2024) to facilitate data exchange among the ILS components.

Catchments equivalent to 15-min rectangular grids (~25 km at the Equator) served as the basic modeling units. A resolution of 15 min is near the lower end of the spatial ranges widely used by Earth System Models (Bacmeister et al., 2018; Kay et al., 2015) and was considered sufficiently fine to capture land surface processes at the sub-catchment scale. The simulation results are explicitly shown for four catchments that represent homogeneous desert, homogeneous forest, gallery forest, and waterlogging (Figures 3c–3f). The geographical locations and satellite images of the selected catchments are illustrated (Figure 3a). The LAI data for all height bands are shown. The heights above the nearest drainage (HANDs) are specified at both the pixel and height band level. The area percentages of the first and second most common plant functional types at the catchment level, and the dominant plant functional type of each band, are illustrated.

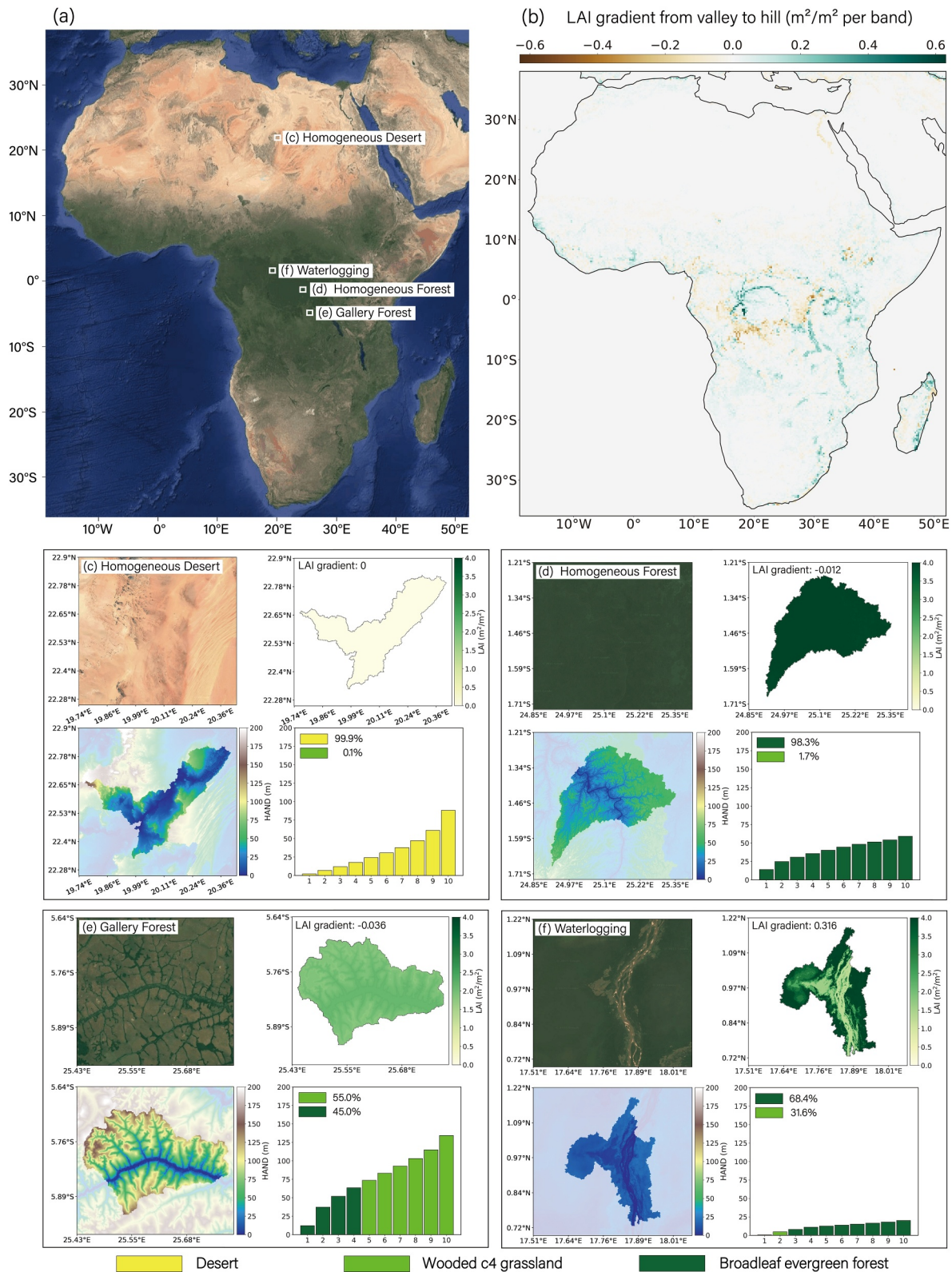


Figure 3.

As lakes and lake depth data were few across the study region, land surface processes over open water were not considered. Catchments in which the dominant land cover type was a water body (a lake or a large river) were excluded.

3.4. Data

The data utilized are summarized in Table 2, including those employed for simulation and validation.

3.4.1. Data for Model Simulation

The MERIT DEM data set yielded the topographic data (Yamazaki et al., 2017) employed to create the boundary conditions for MATSIRO and CaMa-Flood. MERIT Hydro, derived from the MERIT DEM and water body data sets (G1WBM, Global Surface Water Occurrence, and OpenStreetMap), yielded the hydrographic data that represented the hydrographic network (Yamazaki et al., 2019).

MATSIRO requires boundary conditions including the land cover/land use type, soil type, albedo, and LAI. High-resolution land cover data were obtained from the GLCNMO (Kobayashi et al., 2017). Using the 2-m temperature data of JRA55 (Kobayashi et al., 2015), the land cover data were reclassified as plant functional types based on the categorizations of the Simple Biosphere Model 2 (SiB2, Sellers et al., 1996). The details are in Table S1 in Supporting Information S1. Soil types were obtained from the HWSO (FAO & ISRIC, 2012) and were assumed to be uniform throughout each modeling unit. The forest floor albedos were those of ISLSCP I and were classified into visible and near-infrared (Sellers et al., 1996). The 8-day LAIs obtained after re-processing of the MODIS data by Ichii et al. (2017) were resampled to become monthly LAIs with spatial resolutions of 15 arcsec (~500 m at the equator).

The spatial resolution of the climate forcing data was 30 min. Atmospheric forcing data covering the 10-year simulation period (2001–2010) were obtained from GSWP3 (Kim et al., 2016). The data include 3-hourly precipitation (rainfall and snowfall), temperature, shortwave and longwave radiation, surface pressure, specific humidity, and wind speed based on downscaling of the Twentieth-Century Reanalysis (Compo et al., 2011). Cloud cover derived in the same downscaling experiment were used to partition the shortwave radiation into visible/near-infrared components and direct/diffusive components.

The ILS was run for 160 years by cycling the climate forcing 16 times between 2001 and 2010. The first 150 years were used for model spin-up, and the final 10 years for the simulations analysis. The equilibrium status is detailed and illustrated in Text S2 in Supporting Information S1.

3.4.2. Data for Validation

Data from ISMN, FLUXNET, and GRDC stations across the study region from 2001 to 2010 were selected (when available) (Dorigo et al., 2011; Pastorello et al., 2020). Point-based SM observations from ISMN/FLUXNET stations, and Qle and Qh data from FLUXNET stations, have been used to validate MATSIRO simulations directly. The discharges at GRDC stations have been employed to validate discharges simulated by CaMa-Flood directly. In addition, high-resolution LAI data were used to indirectly validate the simulated SMs. The Koppen–Geiger climate map was also employed to validate the SMs of different climatic conditions (Beck et al., 2018).

4. Results

4.1. Modulation of the Land Water and Energy Budgets

In this section, the modeling results of surface SM, runoff, discharge, Qle, and Qh derived with the four experiments are illustrated. As the lake component of MATSIRO was deactivated, continental results were masked

Figure 3. (a) A static Google Earth map showing the geographical details of the African continent; (b) A map of the LAI gradients from valleys to hills within the catchments (the slopes of the linearly fitted lines) where a positive (negative) value indicates relatively low (high) LAI values in the valley compared to the upslope. The four catchments are representative of (c) a homogeneous desert (Touzougou, Libya), (d) a homogeneous forest (Mangu-Mbale, Congo), (e) a gallery forest (Kinda-Mwampu, Congo), and (f) a waterlogging (Mobenzélé, Congo). For each catchment, the static Google Earth map, the LAIs at the various height bands (dotted boundary lines), the HANDs at the pixel and height band levels, the area percentages of the first and second most common plant functional types of the catchments, and the major plant functional type of each height band, are shown.

Table 2
Data Sets Used in This Study

Purpose	Data set	Name	Spatial resolution	Temporal range	Reference
Model simulation	Topography	MERIT DEM	3 arcsec	–	Yamazaki et al. (2017)
	Hydrography	MERIT Hydro	3 arcsec	–	Yamazaki et al. (2019)
	Land Cover	GLCNMO	15 arcsec	2013	Kobayashi et al. (2017)
	2 m Temperature	JRA55	30 min	1958–2013	Kobayashi et al. (2015)
	Soil Type	HWSD	30 arcsec	2008	FAO and ISRIC (2012)
	Surface Albedo	ISLSCP I	60 min	1987–1988	Sellers et al. (1996)
	Leaf Area Index	MODIS	15 arcsec	2000–2016	Ichii et al. (2017)
	Climate Forcings	GSWP3	30 min	1960–2010	Kim et al. (2016)
Validation analysis	Optical Satellite Image	Google static map	–	–	–
	In situ SM	ISMN	Point-based	1952–2024	Dorigo et al. (2011)
	In situ SM, Qle, Qh	FLUXNET	Point-based	1991–2014	Pastorello et al. (2020)
	Discharge gauge data	GRDC	Point-based	1987–2024	–
	Climate Classification	Koppen–Geiger map	30 arcsec	1980–2016	Beck et al. (2018)

when the boundaries delineated water bodies. Since the performance of the default MATSIRO (experiment [2]) were evaluated and summarized in previous studies (Koirala et al., 2012; Nitta et al., 2020; Pokhrel et al., 2012), here we mainly focus on the differences among the experimental results when hillslope heterogeneity was considered.

To facilitate the interpretation of modeling results at the continental scale, we first present outcomes from four representative catchments (Figure 4). For homogeneous desert and homogeneous forest catchments, representing hillslope water and land cover heterogeneities has negligible impact on the catchment-scale water and energy budgets. In contrast, for gallery forest and waterlogging catchments, incorporating these heterogeneities into LSM largely differentiates surface SM, runoff, Qle and Qh along hillslope. For these two catchment types, water and energy budgets vary to different degrees at both the hillslope and catchment levels.

According to Figure 5, when land cover heterogeneity is represented using a tiled scheme, Qle and runoff are affected by changes in canopy area of woody plants. When hillslope water dynamics are resolved, Qle and runoff differ across elevation levels, leading to distinct water and energy budgets at catchment scale. Further incorporating land cover heterogeneity along the hillslope introduces additional modifications to Qle and runoff, as vegetation patterns adapt to the water variability along hillslope. Given the spatial distribution of these two catchment types, the variation patterns in water and energy budgets can be extrapolated to broader regions, thereby informing the interpretation of model results at the continental scale in Sections 4.1.1 and 4.1.2.

4.1.1. Divergence of Modeling Results on Hillslope

The gradients of the intra-annual mean surface SM, runoff, Qle, and Qh from lower to higher bands at the catchment level are shown over the entire African continent in Figure 6, which reveals the divergence of modeling result on hillslope.

When land cover heterogeneity was represented by the tiling scheme in experiment [2], the modeling results exhibited no spatial variability. However, when horizontal water flow became in play in experiment [3], negative hillslope gradients of SM, runoff, and Qle associated with parallel positive hillslope gradients of Qh were observed across extensive areas of equatorial and southern Africa. In the Sahara Desert, which is extremely dry, the hillslope gradients were negligible because the very limited water availability constrained horizontal flow along hillslopes. For example, in the catchment representative of a homogeneous desert, the height band surface SM and runoff reveals little variability among height bands (Figure 4). A similar pattern was observed in the wet and flat Congo Basin. The hillslope gradients were negligible because, as the force of gravity is weak, homogeneous soil saturation of hillslopes substantially reduced horizontal water flow. For example, the catchment representative of homogeneous forest exhibited limited SM and runoff variabilities across the height bands (Figure 4). In comparison, in regions of intermediate water stress with topographic relief (e.g., the Sudanian

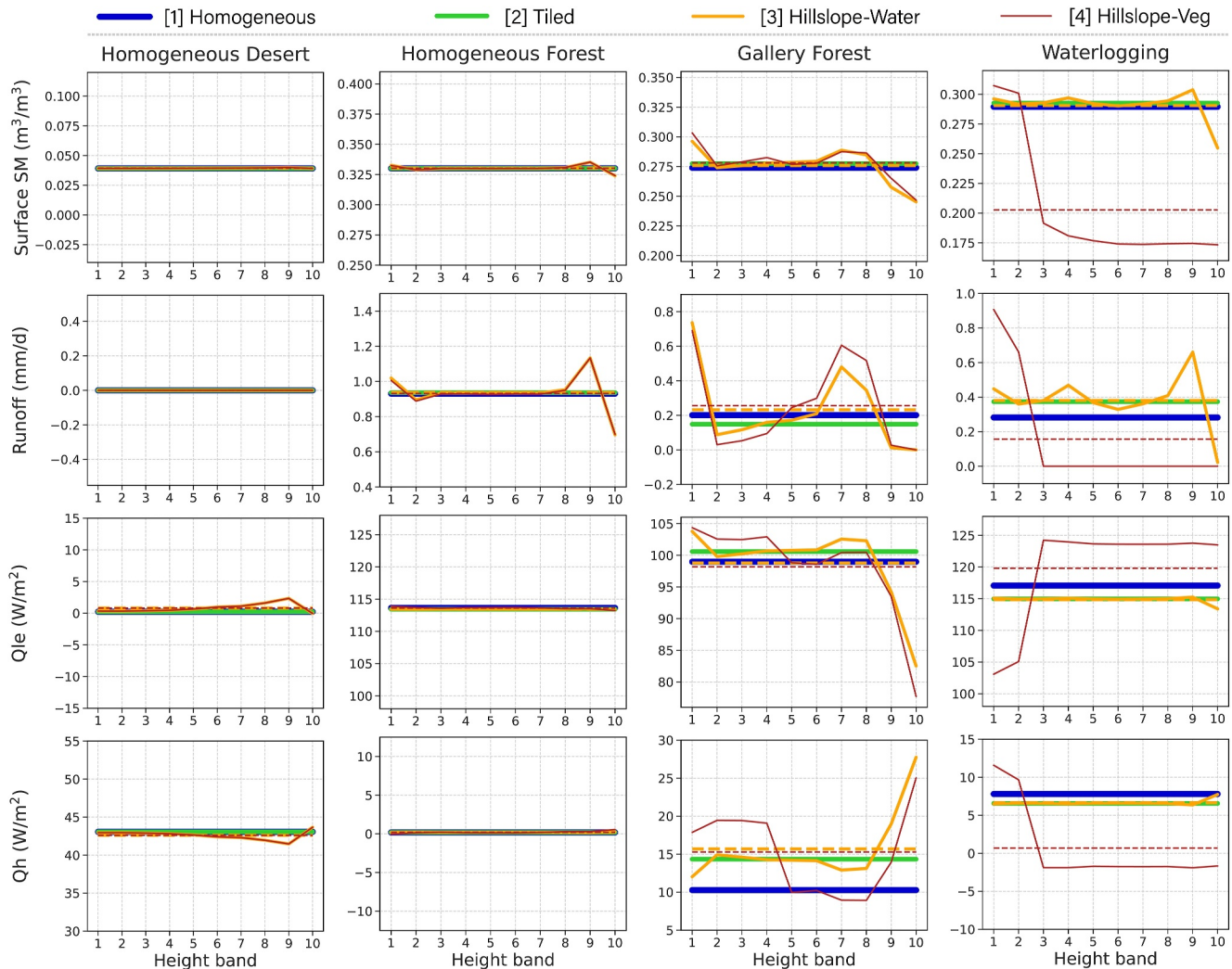


Figure 4. The intra-annual average surface SM, runoff, Qle, and Qh by height bands of the four representative catchments of the four experiments. The horizontal dashed lines in each subplot denote the mean value for all height bands in experiments [3] and [4], respectively. To allow direct comparisons among the simulated SMs, runoffs, and Qle and Qh, the runoff unit has been converted from $\text{kg}/(\text{m}^2\cdot\text{s})$ to mm/d .

Savanna region), the modeling results clearly differed depending on hillslopes. The catchment representative of the gallery forest further exemplified this pattern (Figure 5). Water ran down the hillslope to converge in valleys, associated with wetter valleys and drier hills and thereby negative hillslope wetness gradients. The increasing water availability in valleys enhanced evaporation associated with larger (smaller) Qle (Qh).

Compared to the results of experiment [3], further resolution of the land cover heterogeneity using the catchment-based strategy of experiment [4] revealed additional variations in the hillslope gradient of SM, Qle, and Qh for equatorial Africa ($\Delta([4]-[3])$ in Figure 6). On the one hand, for catchments with denser vegetation on the lower slopes (landscape-type gallery forests, Figures 3e and 5) (Li et al., 2024), explicit representation of the denser woody vegetation on lower hillslopes contributed to more local transpiration and less surface runoff because the canopy intercepted rainfall (Equation 7), which was associated with reduced runoff on land (Figure 5). On the other hand, explicit representation of grasslands on upper hillslopes reduced the canopy area that hindered local transpiration and increased rainfall interception, allowing more terrestrial water to sustain runoff generation (Figure 5). Collectively, these results explain the increasing and decreasing negative hillslope gradients of the simulated Qle and runoff (Figure 6), respectively. However, different hillslope gradient variations were apparent for waterlogging catchments near certain major water bodies (e.g., the Congo River) (Li et al., 2024), where the vegetation tends to be denser on upper hillslopes than elsewhere (Figures 3f and 5). When this was explicitly

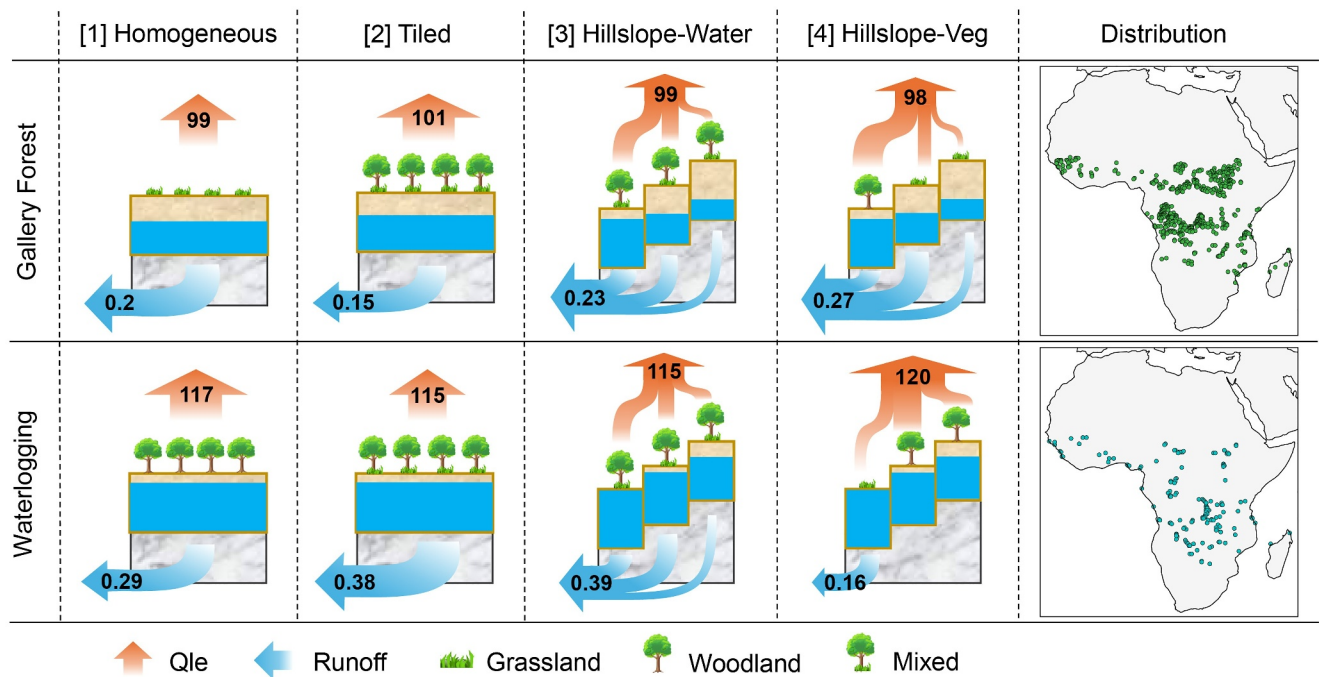


Figure 5. A schematic of Figure 4 summarizing the latent heat flux (Q_{le} , W/m^2) and runoff (mm/d) in gallery forest and waterlogging catchments of four experiments. Numbers on the arrows indicate flux values at the catchment scale, arrow thickness reflects flux magnitude. The main distributions of the two catchment types over Africa are exhibited according to Li et al. (2024).

represented, local transpiration and canopy interception increased, and the sparser vegetation in the valley reduced transpiration and canopy interception (Figure 5). The amounts of water on lower and upper hillslopes increased and decreased respectively, enhancing and constraining runoff generation. Therefore, the Q_{le} hillslope gradient changed from negative in experiment [3] to positive in experiment [4], and those of the SM and runoff exhibited increasingly negative trends in Figure 6.

4.1.2. Differences Among the Experimental Modeling Results

To explore differences among the experimental modeling results at the continental scale, the intra-annual means of experiments [1] and [2] and the average intra-annual means of the 10 height bands of experiments [3] and [4] were compared and mapped over the African continent in terms of SM (Figure 7), runoff (Figure 8), Q_{le} (Figure 9), Q_h (Figure 10) and discharge (Figure 11). In general, SM, runoff, Q_{le} , and Q_h variations were mainly confined to the equatorial regions where the hillslope gradients of LAI were marked (Figure 3b) and gallery forests catchments were common (Figure 5).

4.1.2.1. Resolution of Land Cover Heterogeneity Afforded by Tiling

Compared to experiment [1], in which land cover of each catchment was based only on the dominant type, the land cover heterogeneity was implicitly resolved using the tiling scheme in experiment [2]. This changed the overall canopy areas at the catchment level, especially in semiarid regions.

In the catchment that was representative of homogeneous desert, the dominant land cover type (desert) occupied up to 99.9% of the total area (Figure 3c), explaining the negligible difference in all tested variables across dry northern Africa (Figures 4 and 7–11). This was also the case for the catchment representative of homogeneous forest (Figures 4 and 7–11), where the dominant land cover type (evergreen forest) occupied most of the area (98.3%). For the gallery forest catchments, however, tiling increased the canopy area in the catchment because the second most dominant land cover type (evergreen forest) was explicitly represented (Figure 3e), enhancing Q_{le} and reducing runoff because the canopy intercepted rainfall (Figure 5). In contrast, for waterlogging catchments, tiling decreased the canopy area because the second most dominant land cover type (grassland) was represented (Figure 3f), decreasing the Q_{le} but increasing runoff (Figure 5). These observations explain the Q_{le} (Figure 9) and

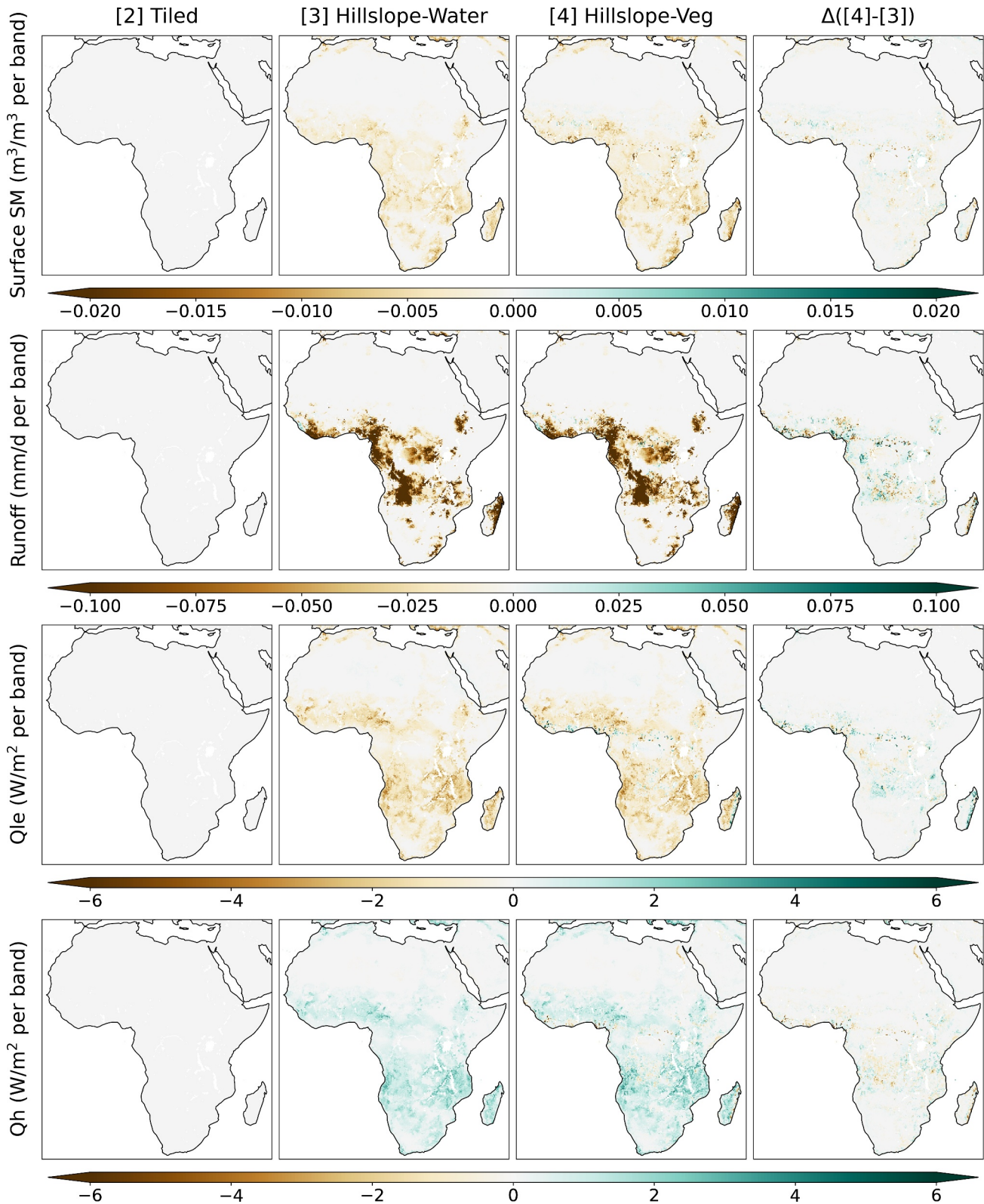
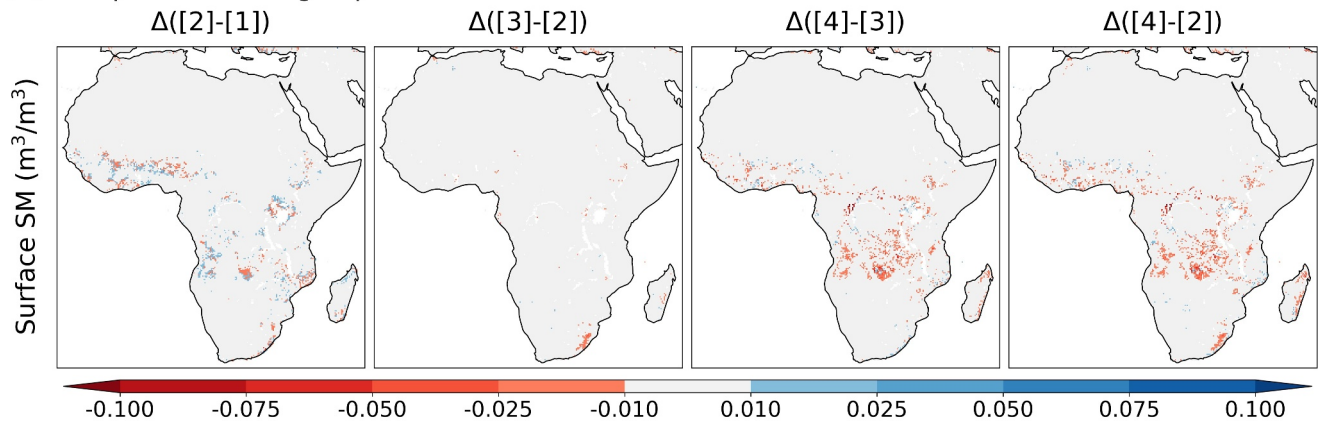
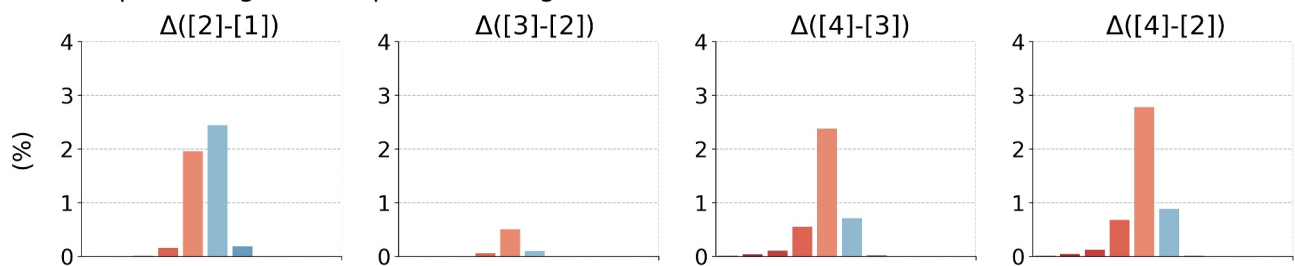


Figure 6. The hillslope gradients of the intra-annual mean surface SM, runoff, Qle, and Qh from lower to higher bands (the slopes of the linearly fitted lines) over the African continent as revealed by experiments [2], [3], and [4] and the differences between experiments [4] and [3]. To allow direct comparisons among the simulated SMs, runoffs, and Qle and Qh, the runoff unit has been converted from $\text{kg}/(\text{m}^2 \cdot \text{s})$ to mm/d .

(a) Comparison among experiments



(b) Area percentage of comparison categories



(c) Comparison of continental mean

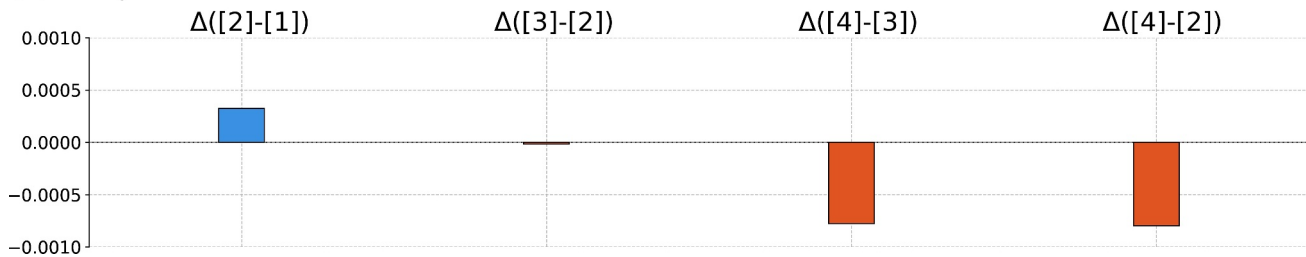


Figure 7. (a) Comparison among the intra-annual mean surface SMs of experiments [1] and [2] and the means of those of the 10 height bands of experiments [3] and [4] over the African continent; (b) the area percentages of the different categories. The colors of the bars match those shown in (a); (c) comparison of the continental mean surface SMs of all four experiments.

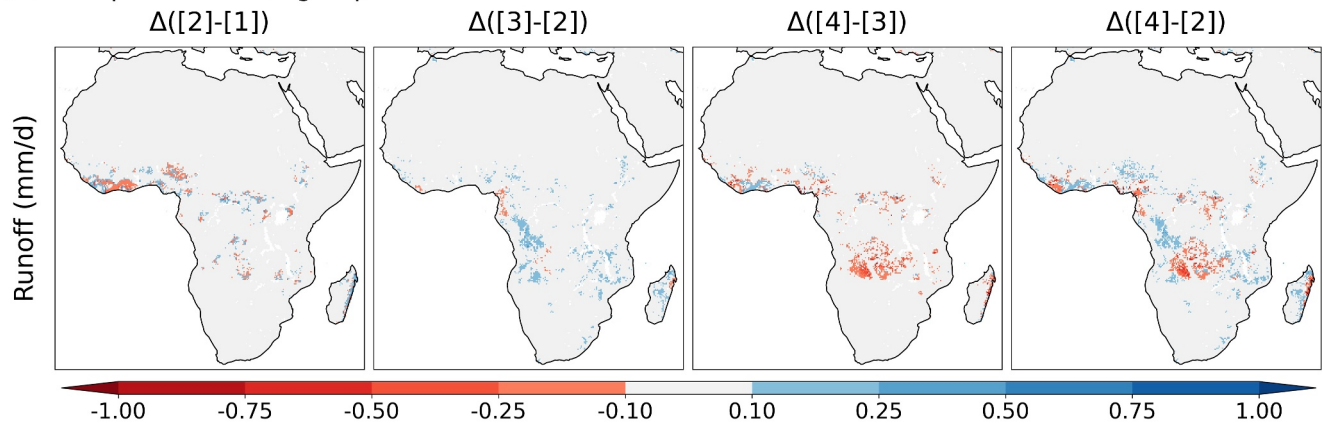
runoff (Figure 8) data across the Congo Basin, the distinctly greater discharges (Figure 11) in the downstream of the Congo River, and the notable increases or decreases in Q_h across a wide range of the southern Congo Basin (Figure 10). In continental terms, tiling increased the African SM, runoff, and Q_h , but decreased the Q_e (Figures 4 and 7–10).

4.1.2.2. Resolution of Hillslope Water Dynamics

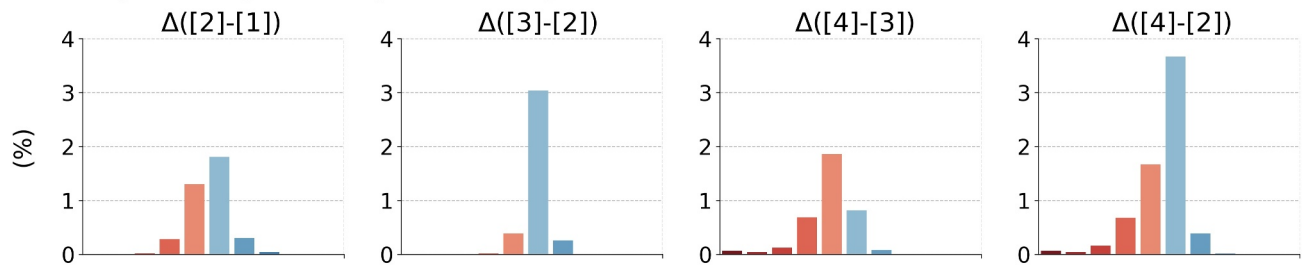
When horizontal water flow became available in experiment [3], it was assumed that water would flow along the hillslope and then down to the valley to create a local water surplus (Figure 6). Compared to that of experiment [2], runoff increased over all of Africa (Figure 8), as did Q_h (Figure 10), but Q_e decreased (Figure 9), particularly near certain major water bodies (e.g., Lake Tanganyika and Lake Malawi).

On the one hand, over the flat terrain of tropical regions that exhibit trivial horizontal water flow and in which energy is relatively limited (e.g., the Congo Basin), hillslopes minimally affected the overall availability of water for evaporation. In mountainous regions, however, water substantially moved to lower hillslopes. Although this minimally affected the Q_e given the already saturated soil, less water was available for evaporation on upper

(a) Comparison among experiments



(b) Area percentage of comparison categories



(c) Comparison of continental mean

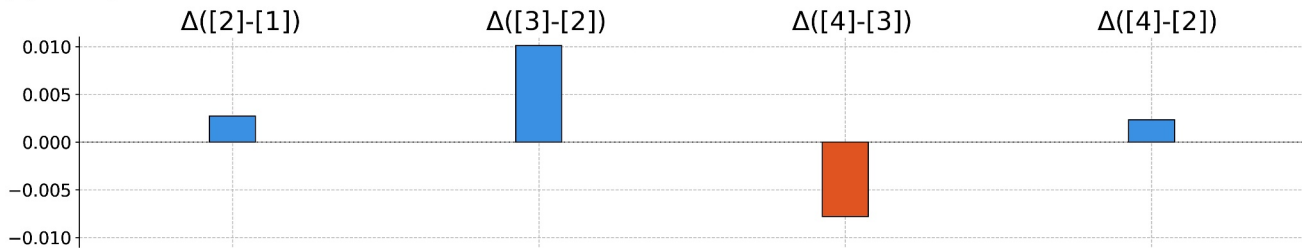


Figure 8. As in Figure 7 with the exception of runoff. To allow direct comparisons among the simulated SMs, runoffs, and Qle and Qh, the runoff unit has been converted from $\text{kg}/(\text{m}^2 \cdot \text{s})$ to mm/d .

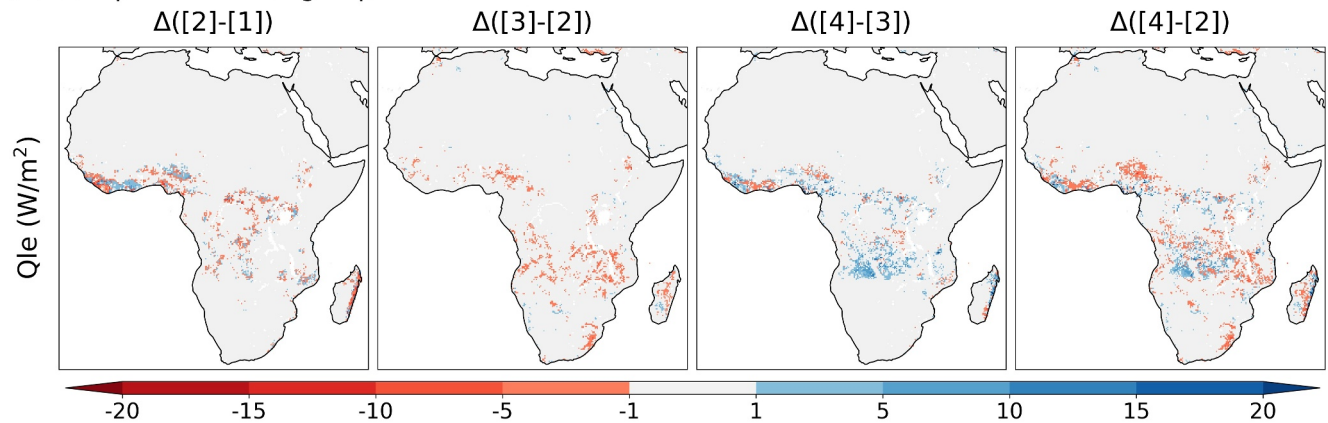
hillslopes (e.g., in the gallery forest of Figure 5). Therefore, the overall catchment Qle decreased. In terms of the SM, despite the hillslope soil water divergence shown in Figure 6, the differences were generally trivial.

On the other hand, a saturated area in a catchment expands when water is received via horizontal flow, except in topographically flat tropical regions. This increases catchment runoff (Figure 8, see references to Equations 6–11). It explains the increased discharge downstream of the Congo River (Figure 11). The various processes described above contribute to greater water loss, increasing the Qh (Figure 10). Interestingly, water surpluses were apparent in certain upper bands in addition to valleys, for example, in the bands of catchments that represented homogeneous desert and forest (Figure 4). This is because, the altitude difference dominated the hydraulic gradient I (Equations 1 and 2): the marked altitude difference greatly enhanced water exchange between neighboring height bands, saturating the soils of lower bands. Similar local phenomena in Switzerland and northern China were described by Pellet and Hauck (2017) and Yan et al. (2024) respectively.

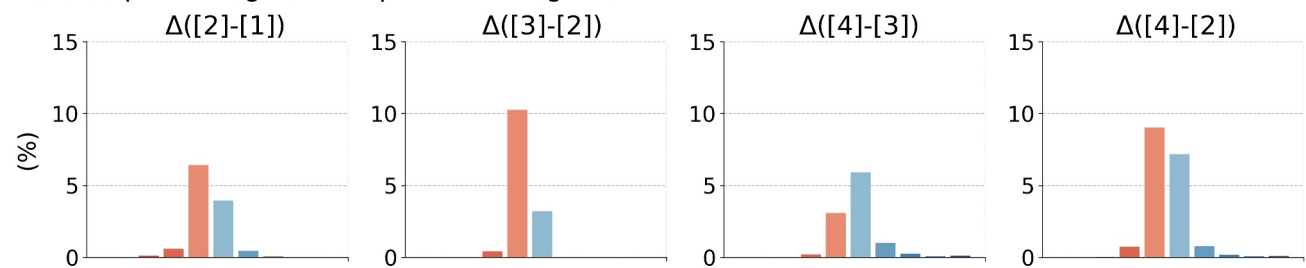
4.1.2.3. Resolution of Land Cover Heterogeneity by Height Bands

Land cover heterogeneity was addressed by the height bands of experiment [4], associated with decreases in the SM (Figure 7), runoff (Figure 8), and Qh (Figure 10); but an increasing Qle (Figure 9), in equatorial Africa. Visual examination revealed locations exhibiting significant variabilities. These overlapped with the catchments

(a) Comparison among experiments



(b) Area percentage of comparison categories



(c) Comparison of continental mean



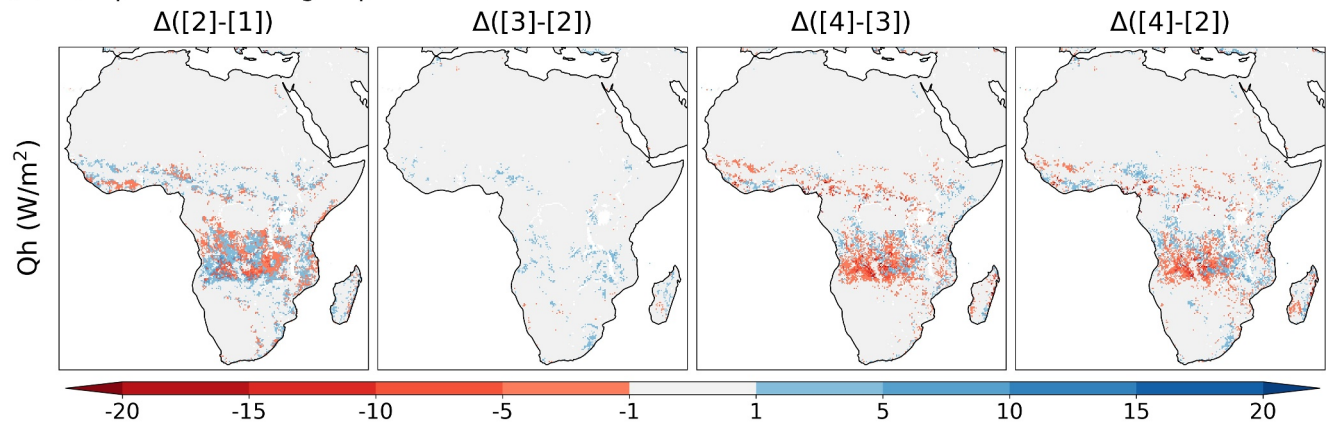
Figure 9. As in Figure 7 with the exception of latent heat flux Qle.

evidencing marked LAI gradients (Figure 3b). The locations were those of gallery forests and waterlogging described in previous study (Li et al., 2024).

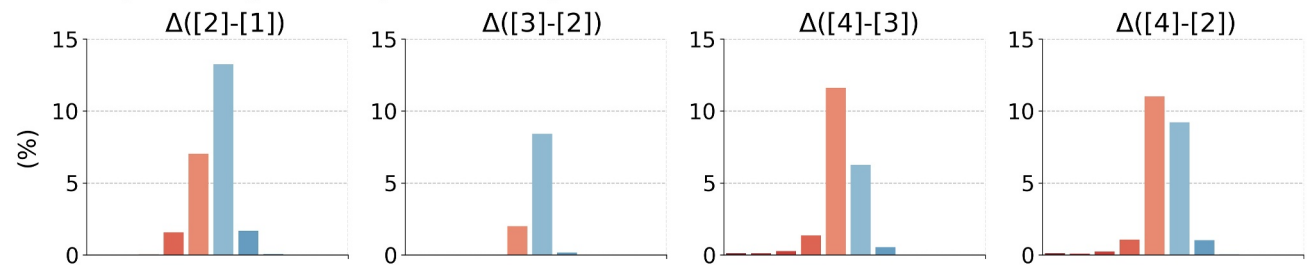
On the one hand, for gallery forest catchments, woody and herbaceous vegetation dominated the lower and upper hillslopes respectively (Figures 3e and 5). When land cover heterogeneity was represented by tiling (Equations 12–14), the second most common land cover type was considered, but this underestimated the extents to which woody vegetation on lower hillslopes reduced local plant transpiration and canopy interception and overestimated how woody vegetation on upper hillslopes enhanced local transpiration and rainfall interception. In contrast, resolution of land cover heterogeneity using height bands homogeneously represented the woody vegetation on lower hillslopes that enhanced (curbed) local Qle (runoff) and the herbaceous vegetation on upper hillslopes that curbed (enhanced) local Qle (runoff) (Figure 5). Notably, subsurface water converged on lower hillslopes to create wetter soils than on upper hillslopes, further increasing the Qle of lower hillslopes and reducing that of upper hillslopes. For the representative catchment shown in Figure 3e, more bands were homogeneously represented by herbaceous vegetation (six bands of the upper hillslope) than by woody vegetation (four bands of the lower hillslope), which reduces Qle and enhances canopy interception on the catchment scale (Figure 5) and was associated with greater water loss from land, leading to less runoff and a higher Qh.

On the other hand, in waterlogging catchments, herbaceous and woody vegetation dominate the lower and upper hillslopes respectively (Figure 3f). Likewise, compared to the tiling scheme, resolution of land cover

(a) Comparison among experiments



(b) Area percentage of comparison categories



(c) Comparison of continental mean

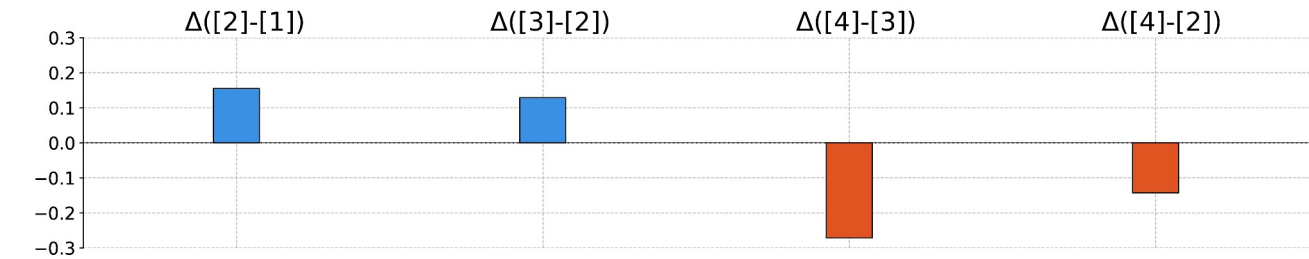


Figure 10. As in Figure 7 with the exception of sensible heat flux Q_h .

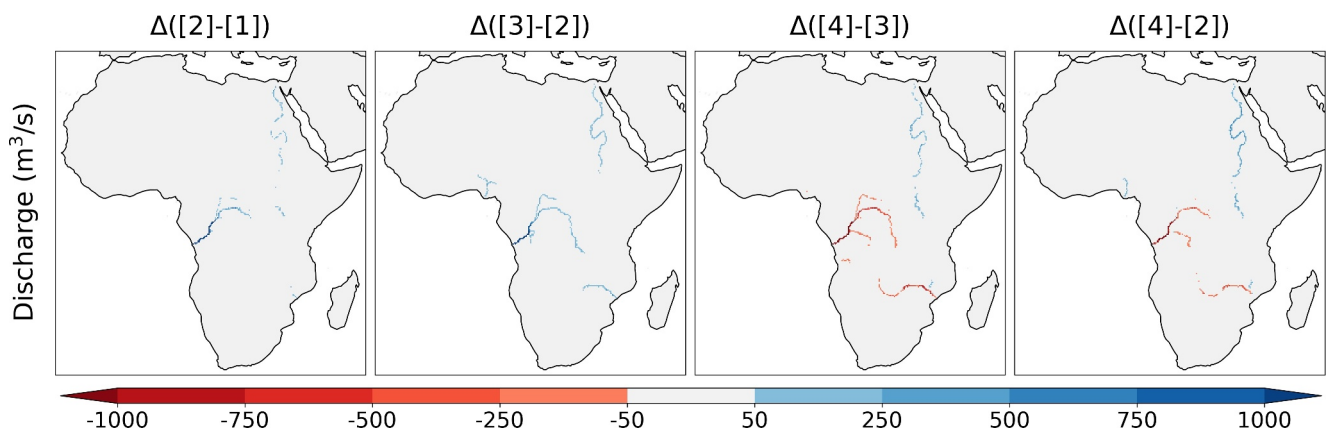


Figure 11. As in Figure 7 with the exception of discharge. The intra-annual means are compared.

heterogeneity using height bands homogeneously represented the herbaceous vegetation of lower hillslopes that curbed (enhanced) local Qle (runoff) and the woody vegetation on upper hillslopes that enhanced (curbed) local Qle (runoff) (Figure 5). However, unlike in gallery forests, where subsurface water converged at lower hillslopes to create wetter soils than those of upper hillslopes, this further decreased the already reduced Qle of lower hillslopes and the enhanced Qle of upper hillslopes. For the representative catchment shown in Figure 3f, more bands were homogeneously represented by woody vegetation (eight bands of the upper hillslope) than by herbaceous vegetation (two bands of the lower hillslope), contributing to the overall increase in Qle and canopy interception at the catchment scale (Figure 5). As a result, land water loss fell, and runoff and Qh increased. Overall, more locations exhibited increasing than decreasing Qle (Figure 9). This, combined with the runoff decreases (Figure 8), explains the reduced discharges to the downstream Congo River (Figure 11).

However, the above processes are not in play in catchments characterized by homogeneous desert and forest because of the homogeneously low or high LAI over the entire catchment (Figure 3c). This explains the negligible differences among all tested variables in the Sahara, Sahel, Namibia Desert and the central Congo Basin. At the sub-catchment level, the simulated SMs were in good spatial agreement with the LAI of the four representative catchments (Figure 13), implying that an LSM representation of land cover heterogeneity that considers the hillslope wetness gradient rendered the simulated SM in excellent alignment with the distributions of woody vegetation.

4.1.2.4. Resolution of Hillslope Water Dynamics and Land Cover Heterogeneity

A comparison of the results of experiments [4] and [2] showed that appropriate consideration of the hillslope water dynamics and land cover heterogeneity revealed differences in the soil water budgets (usually reductions), runoff generation, and energy flux over the African continent, especially in the equatorial regions. The surface SMs ($>0.01 \text{ m}^3/\text{m}^3$) differed in roughly 5% of the study region areas, with 4% and 1% evidencing decreasing and increasing trends respectively (Figure 7). The annual decrease in the surface SM then became $0.0008 \text{ m}^3/\text{m}^3$ across each catchment. In addition, differences in runoff ($>0.1 \text{ mm/d}$) were observed in 7% of the study region areas, with 4% and 3% showing increasing and decreasing trends, respectively (Figure 8), translating to more and less discharge to the mainstem of Nile and Congo Rivers respectively (Figure 11) and annual increases in runoff of $0.002 \text{ m}^3/\text{m}^3$ for each catchment. Also, changes in Qle ($>1 \text{ W/m}^2$) were apparent in 18% of the study areas, of which 10% and 8% were decreases and increases, respectively (Figure 9). Continent-wide, the annual Qle increase was 0.06 W/m^2 for each catchment. Qh budget differences ($>1 \text{ W/m}^2$) were evident for $>22\%$ of the study areas, with 12% and 10% decreasing and increasing, respectively (Figure 10). The overall annual Qh decrease was 0.14 W/m^2 for each catchment.

4.2. Validation of the Modeling Results

4.2.1. Validation of Discharge

Validation of the discharges using the GRDC observations is illustrated in Figure 12. The data of certain GRDC stations were excluded because of abnormally low NSEs (<-1). Some such stations were on the mainstem of large rivers (e.g., Kinshasha downstream on the Congo River). Critical inherent errors in baseline data such as climate forcing may lead to arbitrary modeling characterized by extremely low NSEs, compromising comparisons among different experimental groups. The station NSE data used in the various experiments are shown in Figure 12a, and detailed hydrographs from selected GRDC stations are shown in Figure 12b.

In general, accurately simulated discharges (blue points) were evident at many GRDC stations in all experiments. The overall NSE exhibited a slightly increasing trend as hillslope heterogeneities became better represented from experiment [1] to [4].

Compared to experiment [1], in [2], incorporation of tiling into MATSIRO slightly increased the overall NSE (median NSE rise by 0.05). When the hillslope water dynamics were activated in [3], a further increase in the overall NSE was observed, particularly over the lower quantile of NSEs because, when hillslope water flow was considered, the discharges better captured the observed peak and base flows (Figure 12b; e.g., those at the Senanga, Lukulu, and Mukwe stations). In addition, when changing from the tiling scheme of [3] to the catchment-based strategy of [4] for representation of land cover heterogeneity, the median NSE increased markedly (by 0.07) despite the minor decreases in the upper and lower NSE quantiles.

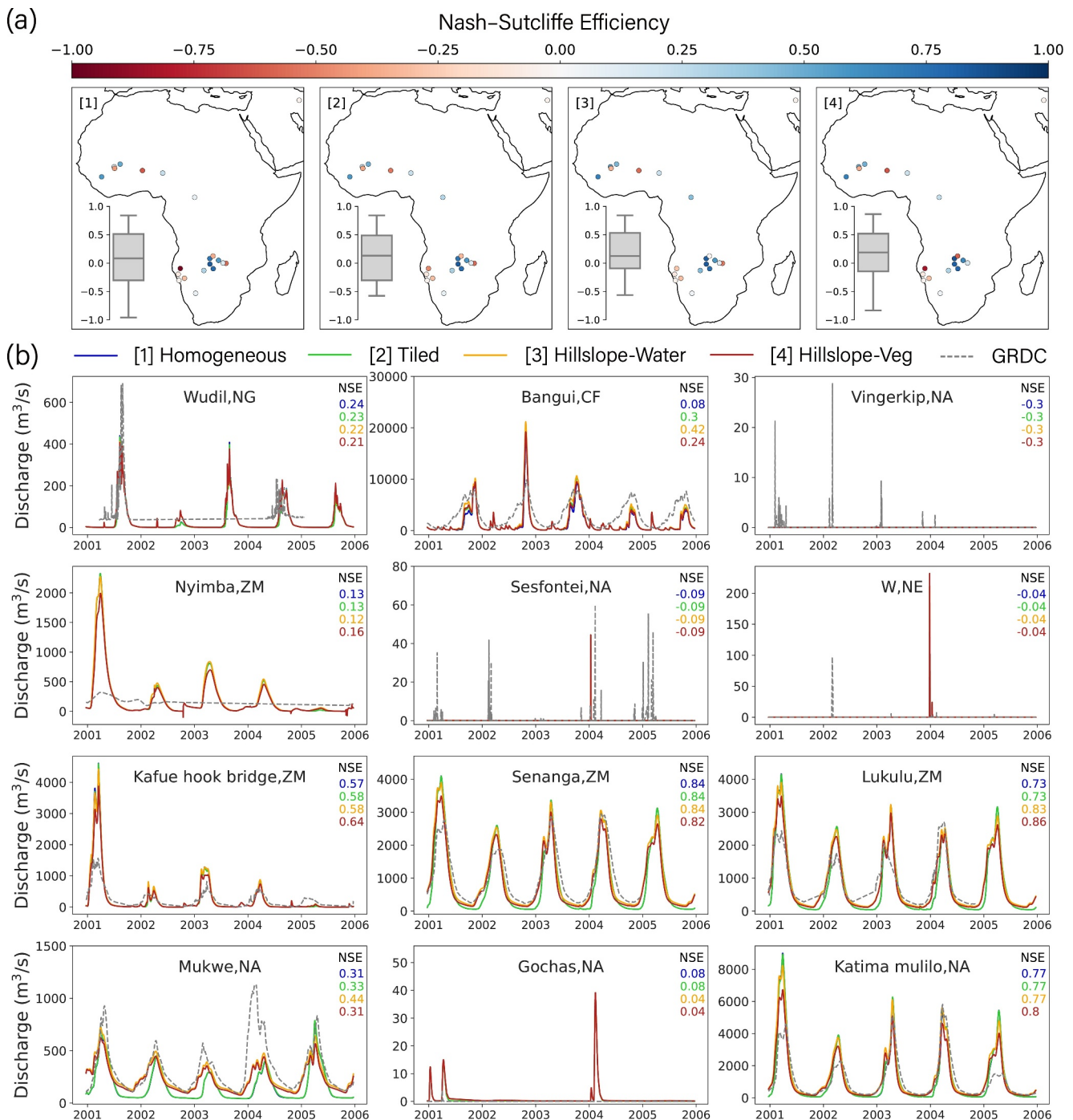


Figure 12. Validation of the simulated discharges over the African continent. (a) Geographical locations of GRDC stations and their NSEs used in the various experiments. The inset box plot summarizes the NSEs of the four experiments. (b) Discharge hydrographs simulated by the ILS for the various experiments and those observed in selected GRDC stations from 2001 to 2005 across the study region (hydrographs for 2001–2010 are shown in Figure S8 in Supporting Information S1). For each subplot, the NSEs were calculated based on the full period and on those derived in the four experiments.

Compared to the simple resolution of the hillslope water dynamics in [3], the simulation results derived after further representation of the hillslope land cover heterogeneity in [4] afforded better agreement with the GRDC observations, alleviating the earlier over- and under-estimations for certain periods (e.g., 2001–2002 in Senanga, 2001–2003 in Lukulu).

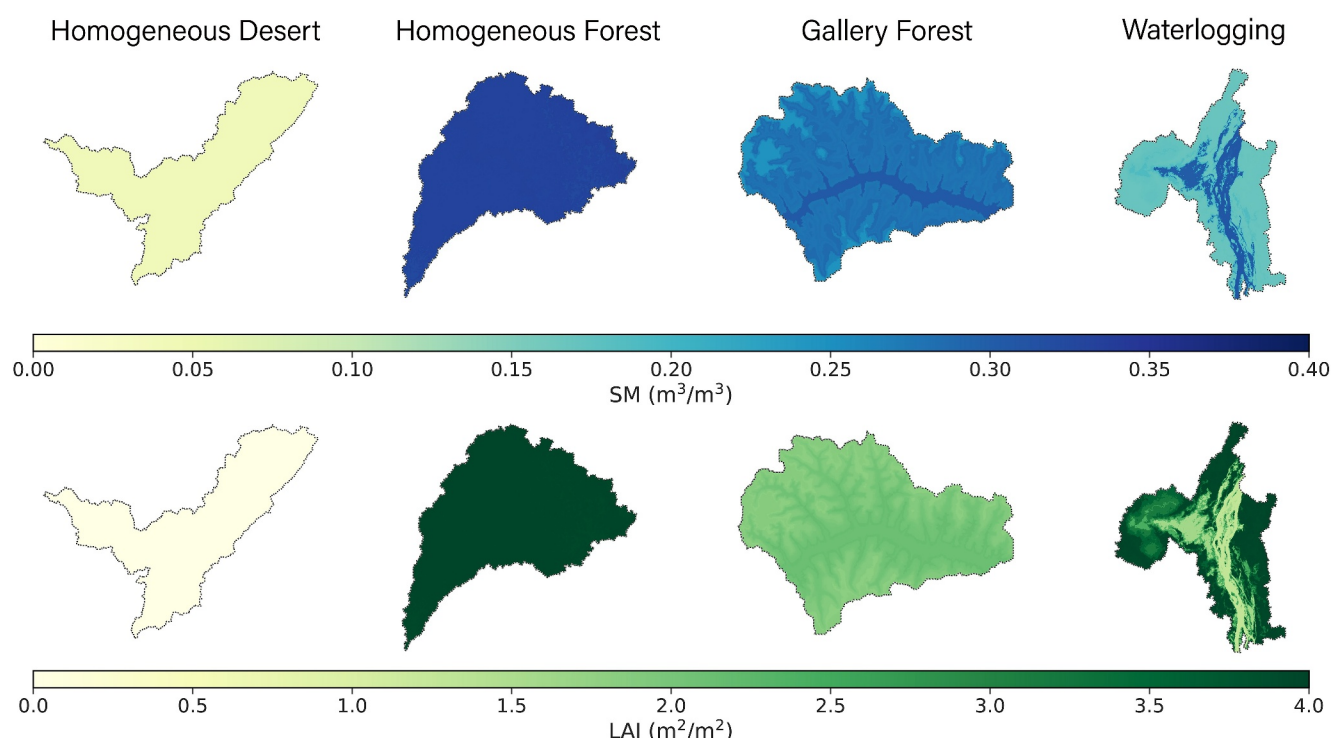


Figure 13. Intra-annual averaged surface SM derived via experiments [4] and the LAI values derived by the height bands of the four representative catchments.

4.2.2. Validation of Soil Moisture

The study using height bands revealed the heterogeneities of the simulated SMs and the observed LAIs on hillslopes (Figure 13). Importantly, on application of catchment-based strategies ([3] and [4]), LAI and SM tend to share similar spatial patterns at the sub-catchment scale. For catchments in semiarid regions (e.g., gallery forests), the associated water stress rendered the simulated SM values relatively high in bands characterized by high rather than low LAIs. For the catchment in a humid (waterlogging) region, higher SMs were observed for upper bands than for lower bands because the relatively high LAI values of the upper bands reflected lower oxygen stress. These two patterns imply that the simulated SMs could alternatively be validated based on the constraint imposed by the soil water content on vegetation growth. In general, there is a critical SM level below which evapotranspiration constrains vegetation growth, but above which excessive soil water suppresses growth (Fu et al., 2022, 2024). That level ranges roughly from $0.12 \text{ m}^3/\text{m}^3$ in arid regions to $0.26 \text{ m}^3/\text{m}^3$ in humid regions, with a global average of $0.19 \text{ m}^3/\text{m}^3$. In this section, the modeling of surface layer SMs in the various experiments' settings is validated using the observed LAI values as the references (Figure 14; the details are in Text S3 in Supporting Information S1).

In tropical regions (Af, Am, and Aw), the median simulated critical SM threshold was $0.2\text{--}0.3 \text{ m}^3/\text{m}^3$ but varied with the experiment, fluctuating around the reference value of $0.26 \text{ m}^3/\text{m}^3$. The simulated critical SM thresholds were generally larger in experiments [1] and [2] than in [3] and [4], and indeed outside the suggested range, especially in the rainforest region (Af), implying SM over-estimation. The critical SM simulated in [3] exhibited a pattern similar to those of [1] and [2] but evidenced better performance in a relatively dry region (Aw), then fitting better within the suggested SM range, indicating the importance of appropriately representing the hillslope water dynamics. On further resolution of the land cover heterogeneity in [4], the simulated critical SM better fitted the suggested values for both rainforest (Af) and monsoon regions (Am), again emphasizing the need to represent hillslope land cover heterogeneity by height bands.

In arid and semiarid regions (BWh, BWk, BSh, and BSk), the simulated critical SMs were generally smaller than in tropical regions, ranging from 0.1 to $0.2 \text{ m}^3/\text{m}^3$ and again varying by the experiment, fluctuating near the reference value of $0.12 \text{ m}^3/\text{m}^3$. Specifically, the simulated critical SM for the desert region (BW) was generally smaller than that for the steppe region (BS). Nevertheless, the simulated critical SMs barely differed among the

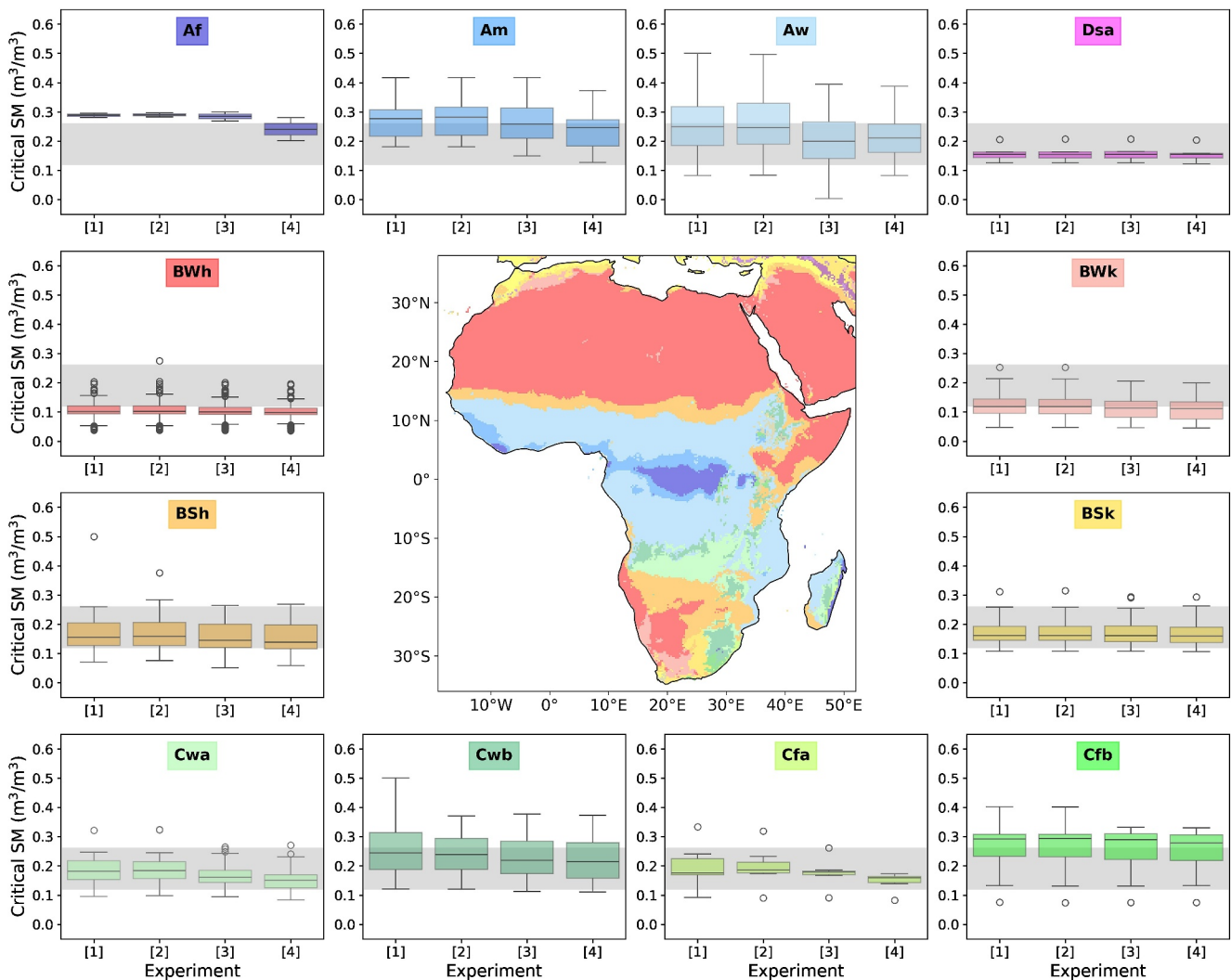


Figure 14. The critical SM values for the different climatic regions of the African continent. In each panel, the background color of the text corresponds to the specific region of the climatic classification map in the middle of the figure, and the light gray area corresponds to the critical SM range suggested by Fu et al. (2024).

four experiments, implying that in dry regions hillslope heterogeneities are not important in the SM context. This was also true of critical SMs simulated for a cold region (Dsa).

In temperate regions (Cwa, Cwb, Cfa, and Cfb), the simulated critical SMs were $0.1\text{--}0.3\text{ m}^3/\text{m}^3$ and fluctuated around the reference value of $0.19\text{ m}^3/\text{m}^3$ in the various experiments, basically well within the suggested range of the critical SM. The relatively wide fluctuation reflected the weaker dominance of SM on LAI in such regions, possibly because anthropogenic and climatic impacts perturbed vegetation growth.

5. Discussion

5.1. Representation of Hillslope Heterogeneity by LSMs

Over the equatorial region of Africa, significant variations in SM, runoff, Qle, and Qh across elevation bands create distinct gradients along hillslopes (Figure 6), in turn influencing the local water conditions that shape hillslope-dominated landscapes such as desert riparian and gallery forests (Li et al., 2024; Rohde et al., 2024). The modeling results accurately reproduced the discharges and SM levels, justifying the assumption that horizontal water dynamics modulate the land surface processes to shape sub-grid land cover heterogeneity (Fan et al., 2019; Li et al., 2024). However, an exception was apparent in the Horn of Africa. Despite the dense existence of desert riparian in this region, the SM, runoff, Qle, and Qh divergences were minor along the hillslopes (Figure 6),

perhaps attributable to the relatively high altitude being associated with a strong climatic impact on the results (von Humboldt, 1807; Li et al., 2024). Consequently, although the effects of hillslopes converged over the lower bands of this catchment, when the data were combined with those of higher bands where climatic factors exert significant impacts (e.g., increasing precipitation caused by orographic lift, associated with local water surpluses in higher bands), the divergence across all bands may be canceled out, yielding only small hillslope gradients.

In previous studies, compared to conventional LSM settings, an overall deeper water table depth and a lower SM were respectively shown by Swenson et al. (2019) and Adachi et al. (2024) when representing the hillslope water dynamics of a global LSM. Using structures similar to those of representative hillslopes (Figure 1), Swenson et al. (2019) and Adachi et al. (2024) simulated the horizontal water flows. Both results implied a trend toward terrestrial water loss. Our simulation results reveal the same pattern and corroborate the previous conclusions. With that being said, the current MATSIRO model addresses hillslope water dynamics within individual catchments but does not account for long-distance water transport at the regional scale. For example, Senay et al. (2014) showed that large areas across the Sudd wetlands in the Nile Basin experience greater evapotranspiration than precipitation, implying substantial horizontal water input at the basin scale. This highlights the need to represent horizontal water dynamics beyond the catchment scale. In addition, current water movement has been unilateral from subsurface layers in MASTIRO to river channel in CaMa-Flood. Swenson et al. (2019) compared hillslope water dynamics predicted by Darcy's law and the kinematic wave theory to find that, in arid regions most soil water accumulation in riparian zones is driven by inflow from river surface water rather than lateral subsurface flow from higher elevations. Future improvements in LSMs should therefore incorporate more realistic representations of groundwater–river channel interactions to enhance subsurface water estimates.

The noteworthy finding is that improvements in the representation of heterogeneous sub-grid water dynamics and land cover consistently resulted in decreasing SM trends. This implies that soil water levels were often overestimated in previous studies that did not employ realistic representation of land cover heterogeneities (Figure 7). Adachi et al. (2024) described an overall decrease in evapotranspiration and increasing runoff over the African continent. Nevertheless, despite the dense vegetation canopies of catchment valleys that clearly contain water, simplifying the representation of land cover heterogeneity tends to underestimate the canopy area and its ability to enhance vegetation transpiration both locally and (possibly) at the catchment scale (Chaney et al., 2018). In light of this, we improved the land cover heterogeneity in LSM and found an overall increase in evapotranspiration and a decrease in runoff at the continental scale, particularly over the equatorial region. Combined with the multi-variable validation of the modeling results (Figures 12 and 14), explicit resolution of land cover heterogeneity along hillslopes yielded results that are in better agreement with the observational data, underscoring the importance of considering hillslope land cover heterogeneity in LSM.

5.2. Validation of the Land Surface Model Results

5.2.1. Directly With In-Situ Observations

To justify the assumption that water flows along hillslopes from hilltops to valleys, two catchments with multiple ISMN stations at different height bands were analyzed. The overall SM values were greater in the lower bands than in the higher bands (Figure S9 in Supporting Information S1) although, in catchment iv, the SM of the lowest band was never consistently higher than that of higher bands. Even at the same band height, the SMs observed by stations built on different hillslopes differed. We assume that varying environmental conditions at local scales (e.g., the microclimate and topography) may then dominate the water and energy fluxes (Chow et al., 2006), explaining the SM heterogeneity at similar elevations.

By discretizing each large grid unit into small sub-grid clusters (the catchment-based strategy), the smaller clusters approximated the scales over which in situ stations measure data (Chaney et al., 2018; Nicolai-Shaw et al., 2015). We thus used the available in situ observational data to validate modeling at the sub-grid (height band) level. However, Text S1 in Supporting Information S1 shows that validation of the simulated SM, Qle, and Qh using single point-based observations was less than perfect, perhaps because of gaps between the point-based observations and areal modeling results at various height bands. The environmental conditions near an in situ station are not always representative of those over the broader sub-grid scale, creating scaling errors (Gruber et al., 2013). To close this gap, we argue that a denser implementation of flux towers across Africa in the future will have wide-ranging benefits for improving LSM and understating the sub-grid land surface process.

Given the limited availability of in situ data that validates modeling results at the sub-grid scale, high-resolution satellite observations may be a better option. That being said, current high-resolution satellite data are time-constrained. For example, SMAP has a spatial resolution of ~ 10 km but data are available only from 2015 onwards (Entekhabi et al., 2014). These do not cover the temporal ranges of some climate forcing data such as GSWP3. However, satellite observations would aid model validation when the temporal range of modeling overlaps with that of the observational data.

5.2.2. Indirectly With SM-LAI Relationships

Although the ranges of the simulated critical SMs for vegetation growth defined in this study are in reasonable agreement with prior knowledge (Fu et al., 2024), the values remain to be effectively constrained to a sufficiently narrow range (Figure 14). For example, the critical SM threshold spans the wide range of $0.1\text{--}0.4\text{ m}^3/\text{m}^3$ in sub-tropical regions (climate type Aw of the Koppen–Gerger map; Beck et al., 2018). This implies that the simulated SMs remain poorly validated, and that the sub-grid water budget may be affected by other factors. Land cover aside, some studies have highlighted the importance of incorporating the sub-grid heterogeneity of soil properties and climate into LSMs (Chaney et al., 2018; Fan et al., 2019; Fisher & Koven, 2020; Iseki et al., 2021). For example, variations in hillslope soil properties affect runoff generation (Iseki et al., 2021) and climatic conditions may differ significantly across topographic gradients (Chaney et al., 2018; Fan et al., 2019; Fiddes & Gruber, 2014). Future studies should consider these factors explicitly to understand their impacts on terrestrial water and energy budgets better.

6. Conclusion

In this study, to approximate realistic complex land surface conditions effectively, a catchment-based strategy was applied in the LSM MATSIRO within the ILS framework, and hillslope water dynamics were then modeled as water exchanges among discretized height bands of representative hillslopes. Four experiments were conducted to define the hillslope heterogeneities explicitly in terms of the horizontal water dynamics and land cover. Using the African continent as the test bed, modeling revealed that:

1. Implementation of the catchment-based strategy into an LSM effectively captured the horizontal water dynamics. Compared to the default LSM, addition of a catchment-based routine revealed spatial variabilities in water and energy budgets at the height band level.
2. The hill-to-valley water dynamics aside, more realistic representation of hillslope vegetation via reasonable matching with the differential soil water contents introduced additional spatial variability to the water and energy budgets. We explicitly explored the distribution of the vegetation canopy within each catchment because this either enhances or suppresses transpiration and canopy rainfall interception, ultimately increasing evapotranspiration and reducing runoff at the continental scale, particularly across equatorial Africa.
3. Modeling of hillslope heterogeneities in terms of the horizontal water dynamics and land cover showed that the soil water content, runoff generation, and evapotranspiration varied over 5%, 7%, and 18% of the African continent, respectively.
4. Explicit representation of the hillslope vegetation distribution in LSM yielded results that were generally in better agreement with observational data than was previously the case. On the one hand, discharge was directly validated by in situ observations. The NSE values calculated from available in situ station data exhibited an overall increasing trend when increasing hillslope heterogeneities were considered. On the other hand, the SM values were indirectly validated by the vegetation index. By considering increasing hillslope heterogeneities, the simulated SM that corresponds to the optimal LAI value now aligns more closely with the critical SM value suggested in the literature. The validation results underscore the need to characterize hillslope heterogeneity appropriately. This will reduce biases arising during estimations of total soil water contents and energy fluxes at the continental scale.

Overall, we have shown that incorporation of complex hillslope heterogeneities into an LSM substantially modulated and better captured the terrestrial water and energy budgets than before, offering a new insight into appropriate sub-grid land surface modeling. Given the wide variabilities in land water content and land-atmosphere energy fluxes, we advocate explicit and appropriate treatment of hillslope processes by large-scale Earth system modelers. This study serves as a solid reference not only when assessing climatic impacts on

ecosystems and human societies but also for reassessment of land feedback to the climatic system. This aids systematic error reduction during modeling (Frassoni et al., 2023).

Conflict of Interest

The authors declare no conflicts of interest relevant to this study.

Data Availability Statement

The MERIT DEM topography data is accessible at https://hydro.iis.u-tokyo.ac.jp/~yamada/MERIT_DEM/. The MERIT Hydro hydrography data is accessible at https://hydro.iis.u-tokyo.ac.jp/~yamada/MERIT_Hydro/. The GLCNMO land cover data set is downloaded from <https://globalmaps.github.io/glcnm.html>. JRA55 reanalysis data is acquired at https://jra.kishou.go.jp/JRA-55/index_en.html. HWSD soil type data is retrieved from <https://www.fao.org/soils-portal/data-hub/soil-maps-and-databases/harmonized-world-soil-database-v20/en/>. ISLSCP I Surface albedo data is accessible at <https://catalogue.ceda.ac.uk/uuid/48c9cd8b8dd43490c8d786a28e9c1a44/>. The MODIS LAI data are obtained from <ftp://modis.cr.chiba-u.ac.jp/ichii/DATA/MODIS/GLOBAL/tmp/>. The GSWP3 climate forcing data is available at <https://www.isimip.org/gettingstarted/input-data-bias-adjustment/details/4/>. The ISMN in situ SM data is, after registration of an account in the platform, freely accessible through <https://ismn.earth/en/>. The FLUXNET in situ data is also freely available at <https://fluxnet.org/about/> after account registration. The GRDC discharge observation data can be downloaded at <https://grdc.bafg.de/> when request is permitted. The Köppen–Geiger climate map is available at <https://www.gloh2o.org/koppen/>. All links are valid as of 19 August 2025.

Acknowledgments

We thank the anonymous reviewer for giving constructive comments to improve the manuscript. This research was supported by the JSPS KAKENHI (21H05002, 22H04938), MEXT program for the advanced studies of climate change projection SENTAN (JPMXD0722680395, JPMXD1420318865), the Environment Research and Technology Development Fund S-20 of the Environmental Restoration and Conservation Agency of Japan (JPMEERF21S12020), Earth Observation Research Center, Japan Aerospace Exploration Agency (JX-PSPC-533980), JST-Mirai Program (JPMJMI2116), JST-Moonshot Program (JPMJMS2282-08), JST-eASIA Joint Research Program (JPMJSC22E4), Kurata Fund of Hitachi Global Foundation in the year 2024.

References

- Adachi, K., Yamazaki, D., & Nitta, T. (2024). Represent hill–valley moisture contrast by land surface model with lateral subsurface flow. *Journal of JSCE*, 12(1), 23–00232. <https://doi.org/10.2208/journalofjsce.23-00232>
- Ajami, H., Khan, U., Tuteja, N. K., & Sharma, A. (2016). Development of a computationally efficient semi-distributed hydrologic modeling application for soil moisture, lateral flow and runoff simulation. *Environmental Modelling & Software*, 85, 319–331. <https://doi.org/10.1016/j.envsoft.2016.09.002>
- Arakawa, T., Inoue, T., Yashiro, H., & Satoh, M. (2020). Coupling library Jcup3: Its philosophy and application. *Progress in Earth and Planetary Science*, 7(1), 1–17. <https://doi.org/10.1186/s40645-019-0320-z>
- Bacmeister, J. T., Reed, K. A., Hannay, C., Lawrence, P., Bates, S., Truesdale, J. E., et al. (2018). Projected changes in tropical cyclone activity under future warming scenarios using a high-resolution climate model. *Climatic Change*, 146(3), 547–560. <https://doi.org/10.1007/s10584-016-1750-x>
- Bates, P. D., Horritt, M. S., & Fewtrell, T. J. (2010). A simple inertial formulation of the shallow water equations for efficient two-dimensional flood inundation modelling. *Journal of Hydrology*, 387(1), 33–45. <https://doi.org/10.1016/j.jhydrol.2010.03.027>
- Beck, H. E., Zimmermann, N. E., McVicar, T. R., Vergopolan, N., Berg, A., & Wood, E. F. (2018). Present and future Köppen–Geiger climate classification maps at 1-km resolution. *Scientific Data*, 5, 1–12. <https://doi.org/10.1038/sdata.2018.214>
- Beven, K. J., & Kirkby, M. J. (1979). A physically based, variable contributing area model of basin hydrology/Un modèle à base physique de zone d'appel variable de l'hydrologie du bassin versant. *Hydrological Sciences Journal*, 24(1), 43–69. <https://doi.org/10.1080/02626667909491834>
- Bierkens, M. F. P. (2015). Global hydrology 2015: State, trends, and directions. *Water Resources Research*, 51(7), 4923–4947. <https://doi.org/10.1002/2015wr017173>
- Brooks, P. D., Chorover, J., Fan, Y., Godsey, S. E., Maxwell, R. M., McNamara, J. P., & Tague, C. (2015). Hydrological partitioning in the critical zone: Recent advances and opportunities for developing transferable understanding of water cycle dynamics. *Water Resources Research*, 51(9), 6973–6987. <https://doi.org/10.1002/2015wr017039>
- Burton, C., Betts, R., Cardoso, M., Feldpausch, T. R., Harper, A., Jones, C. D., et al. (2019). Representation of fire, land-use change and vegetation dynamics in the joint UK land environment simulator vn4. 9 (JULES). *Geoscientific Model Development*, 12(1), 179–193. <https://doi.org/10.5194/gmd-12-179-2019>
- Byrne, M. P., Hegerl, G. C., Scheff, J., Adam, O., Berg, A., Biasutti, M., et al. (2024). Theory and the future of land-climate science. *Nature Geoscience*, 17(11), 1079–1086. <https://doi.org/10.1038/s41561-024-01553-8>
- Chaney, N. W., Huijgevoort, M. H. J. V., Shevliakova, E., Malyshev, S., Milly, P. C. D., Gauthier, P. P. G., & Sulman, B. N. (2018). Harnessing big data to rethink land heterogeneity in Earth system models. *Hydrology and Earth System Sciences*, 22(6), 3311–3330. <https://doi.org/10.5194/hess-22-3311-2018>
- Chow, F. K., Weigel, A. P., Street, R. L., Rotach, M. W., & Xue, M. (2006). High-resolution large-eddy simulations of flow in a steep Alpine valley. Part I: Methodology, verification, and sensitivity experiments. *Journal of Applied Meteorology and Climatology*, 45(1), 63–86. <https://doi.org/10.1175/jam2322.1>
- Clark, M. P., Fan, Y., Lawrence, D. M., Adam, J. C., Bolster, D., Gochis, D. J., et al. (2015). Improving the representation of hydrologic processes in Earth SystemModels (pp. 5929–5956). <https://doi.org/10.1002/2015WR017096>
- Compo, G. P., Whitaker, J. S., Sardeshmukh, P. D., Matsui, N., Allan, R. J., Yin, X., et al. (2011). The twentieth century reanalysis project. *Quarterly Journal of the Royal Meteorological Society*, 137(654), 1–28. <https://doi.org/10.1002/qj.776>
- Dickinson, R. E. (1984). Modeling evapotranspiration for three-dimensional global climate models. *Climate Processes and Climate Sensitivity*, 29, 58–72. <https://doi.org/10.1029/gm029p0058>

- Dorigo, W. A., Wagner, W., Hohensinn, R., Hahn, S., Paulik, C., Xaver, A., et al. (2011). The international soil moisture network: A data hosting facility for global in situ soil moisture measurements. *Hydrology and Earth System Sciences*, 15(5), 1675–1698. <https://doi.org/10.5194/hess-15-1675-2011>
- Entekhabi, D., Yueh, S., & De Lannoy, G. (2014). SMAP handbook.
- Fan, Y., Clark, M., Lawrence, D. M., Swenson, S., Band, L. E., Brantley, S. L., et al. (2019). Hillslope hydrology in global change research and Earth system modeling. *Water Resources Research*, 55(2), 1737–1772. <https://doi.org/10.1029/2018WR023903>
- Fao, I., & Isric, I. (2012). *Jrc: Harmonized world soil database (version 1.2)*. FAO, Rome, Italy and IIASA, Laxenburg, Austria.
- Farquhar, G. D., von Caemmerer, S., & Berry, J. A. (1980). A biochemical model of photosynthetic CO₂ assimilation in leaves of C₃ species. *Planta*, 149(1), 78–90. <https://doi.org/10.1007/bf00386231>
- Fiddes, J., & Gruber, S. (2014). TopoSCALE v.1.0: Downscaling gridded climate data in complex terrain. *Geoscientific Model Development*, 7(1), 387–405. <https://doi.org/10.5194/gmd-7-387-2014>
- Fisher, R. A., & Koven, C. D. (2020). Perspectives on the future of land surface models and the challenges of representing complex terrestrial systems. *Journal of Advances in Modeling Earth Systems*, 12(4), e2018MS001453. <https://doi.org/10.1029/2018MS001453>
- Fox, A. M., Huntley, B., Lloyd, C. R., Williams, M., & Baxter, R. (2008). Net ecosystem exchange over heterogeneous Arctic tundra: Scaling between chamber and eddy covariance measurements. *Global Biogeochemical Cycles*, 22(2), GB2027. <https://doi.org/10.1029/2007gb003027>
- Frasson, A., Reynolds, C., Wedi, N., Bouallègue, Z. B., Caltabiano, A. C. V., Casati, B., et al. (2023). Systematic errors in weather and climate models: Challenges and opportunities in complex coupled modeling systems. *Bulletin of the American Meteorological Society*, 104(9), E1687–E1693. <https://doi.org/10.1175/bams-d-23-0102.1>
- Fu, Z., Ciais, P., Feldman, A. F., Gentile, P., Makowski, D., Prentice, I. C., et al. (2022). Critical soil moisture thresholds of plant water stress in terrestrial ecosystems. *Science Advances*, 8(44), 1–13. <https://doi.org/10.1126/sciadv.abq7827>
- Fu, Z., Ciais, P., Wigneron, J.-P., Gentile, P., Feldman, A. F., Makowski, D., et al. (2024). Global critical soil moisture thresholds of plant water stress. *Nature Communications*, 15(1), 4826. <https://doi.org/10.1038/s41467-024-49244-7>
- Gruber, A., Dorigo, W. A., Zwieback, S., Xaver, A., & Wagner, W. (2013). Characterizing coarse-scale representativeness of in situ soil moisture measurements from the international soil moisture network. *Vadose Zone Journal*, 12(2), vzj2012.0170. <https://doi.org/10.2136/vzj2012.0170>
- Hasumi, H., & Emori, S. (2004). *K-1 coupled model (MIROC) description* (Vol. 34). Center for Climate System Research, University of Tokyo K-1 Technical Report.
- Ichii, K., Ueyama, M., Kondo, M., Saigusa, N., Kim, J., Alberto, M. C., et al. (2017). New data-driven estimation of terrestrial CO₂ fluxes in Asia using a standardized database of eddy covariance measurements, remote sensing data, and support vector regression. *Journal of Geophysical Research: Biogeosciences*, 122(4), 767–795. <https://doi.org/10.1002/2016JG003640>
- Iseki, K., Ikazaki, K., & Batieno, J. B. (2021). Cowpea yield variation in three dominant soil types in the Sudan Savanna of West Africa. *Field Crops Research*, 261, 108012. <https://doi.org/10.1016/j.fcr.2020.108012>
- Kay, J. E., Deser, C., Phillips, A., Mai, A., Hannay, C., Strand, G., et al. (2015). The community earth system model (CESM) large ensemble project: A community resource for studying climate change in the presence of internal climate variability. *Bulletin of the American Meteorological Society*, 96(8), 1333–1349. <https://doi.org/10.1175/bams-d-13-00255.1>
- Kim, H., Watanabe, S., Chang, E. C., Yoshimura, K., Compo, G. P., Hirabayashi, Y., et al. (2016). A century-long global surface meteorology for offline terrestrial simulations. preparation.
- Kobayashi, S., Ota, Y., Harada, Y., Ebata, A., Moriya, M., Onoda, H., et al. (2015). The JRA-55 reanalysis: General specifications and basic characteristics. *Journal of the Meteorological Society of Japan. Ser. II*, 93(1), 5–48. <https://doi.org/10.2151/jmsj.2015-001>
- Kobayashi, T., Tateishi, R., Alsaadeh, B., Sharma, R. C., Wakaizumi, T., Miyamoto, D., et al. (2017). Production of global land cover data—GLCNMO2013. *Journal of Geography and Geology*, 9(3), 1–15. <https://doi.org/10.5539/jgg.v9n3p1>
- Koirala, S., Yamada, H., Yeh, P., Oki, T., Hirabayashi, Y., & Kanae, S. (2012). Global simulation of groundwater recharge, water table depth, and low flow using a land surface model with groundwater representation. *Journal of Japan Society of Civil Engineers, Ser. B1 (Hydraulic Engineering)*, 68(4), I_211–I_216. https://doi.org/10.2208/jsejhe.68.i_211
- Lawrence, D. M., Fisher, R. A., Koven, C. D., Oleson, K. W., Swenson, S. C., Bonan, G., et al. (2019). The community land model version 5: Description of new features, benchmarking, and impact of forcing uncertainty. *Journal of Advances in Modeling Earth Systems*, 11(12), 4245–4287. <https://doi.org/10.1029/2018MS001583>
- Li, S., Yamazaki, D., Zhou, X., & Zhao, G. (2024). Where in the world are vegetation patterns controlled by hillslope water dynamics? *Water Resources Research*, 60(4), e2023WR036214. <https://doi.org/10.1029/2023WR036214>
- Lundquist, J. D., & Dettinger, M. D. (2005). How snowpack heterogeneity affects diurnal streamflow timing. *Water Resources Research*, 41(5), W05007. <https://doi.org/10.1029/2004wr003649>
- Manabe, S. (1969). Climate and the ocean circulation: I. The atmospheric circulation and the hydrology of the earth's surface. *Monthly Weather Review*, 97(11), 739–774. [https://doi.org/10.1175/1520-0493\(1969\)097<0739:catoc>2.3.co;2](https://doi.org/10.1175/1520-0493(1969)097<0739:catoc>2.3.co;2)
- MATSIRO6 Document Writing Team. (2021). Description of MATSIRO6. <https://doi.org/10.15083/0002000181>
- Milly, P. C. D., Malyshev, S. L., Shevliakova, E., Dunne, K. A., Findell, K. L., Gleeson, T., et al. (2014). An enhanced model of land water and energy for global hydrologic and earth-system studies. *Journal of Hydrometeorology*, 15(5), 1739–1761. <https://doi.org/10.1175/jhm-d-13-0162.1>
- Nash, J. E., & Sutcliffe, J. V. (1970). River flow forecasting through conceptual models part I — A discussion of principles. *Journal of Hydrology*, 10(3), 282–290. [https://doi.org/10.1016/0022-1694\(70\)90255-6](https://doi.org/10.1016/0022-1694(70)90255-6)
- Naudts, K., Ryder, J., McGrath, M. J., Otto, J., Chen, Y., Valade, A., et al. (2015). A vertically discretised canopy description for ORCHIDEE (SVN r2290) and the modifications to the energy, water and carbon fluxes. *Geoscientific Model Development*, 8(7), 2035–2065. <https://doi.org/10.5194/gmd-8-2035-2015>
- Ngo-Duc, T., Laval, K., Ramillien, G., Polcher, J., & Cazenave, A. (2007). Validation of the land water storage simulated by organising carbon and hydrology in dynamic ecosystems (ORCHIDEE) with gravity recovery and climate experiment (GRACE) data. *Water Resources Research*, 43(4), W04427. <https://doi.org/10.1029/2006wr004941>
- Nicolai-Shaw, N., Hirschi, M., Mittelbach, H., & Seneviratne, S. I. (2015). Spatial representativeness of soil moisture using in situ, remote sensing, and land reanalysis data. *Journal of Geophysical Research: Atmospheres*, 120(19), 9955–9964. <https://doi.org/10.1002/2015JD023305>
- Nitta, T., Arakawa, T., Hatono, M., Takeshima, A., & Yoshimura, K. (2020). Development of integrated land simulator. *Progress in Earth and Planetary Science*, 7(1), 68. <https://doi.org/10.1186/s40645-020-00383-7>
- Pastorello, G., Trotta, C., Canfora, E., Chu, H., Christianson, D., Cheah, Y.-W., et al. (2020). The FLUXNET2015 dataset and the ONEFlux processing pipeline for eddy covariance data. *Scientific Data*, 7(1), 225. <https://doi.org/10.1038/s41597-020-0534-3>

- Pellet, C., & Hauck, C. (2017). Monitoring soil moisture from middle to high elevation in Switzerland: Set-up and first results from the SOMOMOUNT network. *Hydrology and Earth System Sciences*, 21(6), 3199–3220. <https://doi.org/10.5194/hess-21-3199-2017>
- Pokhrel, Y., Hanasaki, N., Koirala, S., Cho, J., Yeh, P. J.-F., Kim, H., et al. (2012). Incorporating anthropogenic water regulation modules into a land surface model. *Journal of Hydrometeorology*, 13(1), 255–269. <https://doi.org/10.1175/jhm-d-11-013.1>
- Rohde, M. M., Albano, C. M., Huggins, X., Klausmeyer, K. R., Morton, C., Sharman, A., et al. (2024). Groundwater-dependent ecosystem map exposes global dryland protection needs. *Nature*, 632(8023), 101–107. <https://doi.org/10.1038/s41586-024-07702-8>
- Sellers, P. J., Meeson, B. W., Closs, J., Collatz, J., Corprew, F., Dazlich, D., et al. (1996). The ISLSCP initiative I global datasets: Surface boundary conditions and atmospheric forcings for land-atmosphere studies. *Bulletin of the American Meteorological Society*, 77(9), 1987–2006. [https://doi.org/10.1175/1520-0477\(1996\)077<1987:tiignd>2.0.co;2](https://doi.org/10.1175/1520-0477(1996)077<1987:tiignd>2.0.co;2)
- Sellers, P. J., Mintz, Y., Sud, Y. C., & Dalcher, A. (1986). A simple biosphere model (SiB) for use within general circulation models. *Journal of the Atmospheric Sciences*, 43(6), 505–531. [https://doi.org/10.1175/1520-0469\(1986\)043<0505:asbmfu>2.0.co;2](https://doi.org/10.1175/1520-0469(1986)043<0505:asbmfu>2.0.co;2)
- Senay, G. B., Velpuri, N. M., Bohms, S., Demissie, Y., & Gebremichael, M. (2014). Understanding the hydrologic sources and sinks in the Nile Basin using multisource climate and remote sensing data sets. *Water Resources Research*, 50(11), 8625–8650. <https://doi.org/10.1002/2013wr015231>
- Simpson, I. R., McKinnon, K. A., Kennedy, D., Lawrence, D. M., Lehner, F., & Seager, R. (2024). Observed humidity trends in dry regions contradict climate models. *Proceedings of the National Academy of Sciences*, 121(1), e2302480120. <https://doi.org/10.1073/pnas.2302480120>
- Stephens, G., Polcher, J., Zeng, X., van Oevelen, P., Poveda, G., Bosilovich, M., et al. (2023). The first 30 years of GEWEX. *Bulletin of the American Meteorological Society*, 104(1), E126–E157. <https://doi.org/10.1175/BAMS-D-22-0061.1>
- Stieglitz, M., Rind, D., Famiglietti, J., & Rosenzweig, C. (1997). An efficient approach to modeling the topographic control of surface hydrology for regional and global climate modeling. *Journal of Climate*, 10(1), 118–137. [https://doi.org/10.1175/1520-0442\(1997\)010<0118:aeatmt>2.0.co;2](https://doi.org/10.1175/1520-0442(1997)010<0118:aeatmt>2.0.co;2)
- Subin, Z. M., Milly, P. C. D., Sulman, B. N., Malyshev, S., & Shevliakova, E. (2014). Resolving terrestrial ecosystem processes along a subgrid topographic gradient for an earth-system model. *Hydrology and Earth System Sciences Discussions*, 11(7), 8443–8492.
- Swenson, S. C., Clark, M., Fan, Y., Lawrence, D. M., & Perket, J. (2019). Representing intrahillslope lateral subsurface flow in the community land model. *Journal of Advances in Modeling Earth Systems*, 11(12), 4044–4065. <https://doi.org/10.1029/2019MS001833>
- Tai, X., Mackay, D. S., Anderegg, W. R. L., Sperry, J. S., & Brooks, P. D. (2017). Plant hydraulics improves and topography mediates prediction of aspen mortality in southwestern USA. *New Phytologist*, 213(1), 113–127. <https://doi.org/10.1111/nph.14098>
- Takata, K., Emori, S., & Watanabe, T. (2003). Development of the minimal advanced treatments of surface interaction and runoff. *Global and Planetary Change*, 38(1–2), 209–222. [https://doi.org/10.1016/S0921-8181\(03\)00030-4](https://doi.org/10.1016/S0921-8181(03)00030-4)
- Takeshima, A., & Yoshimura, K. (2024). Application of catchment-based grid to land model in the Aogcm-Lsm coupled system. *Japanese Journal of JSCE*, 80(16), 23–16097. <https://doi.org/10.2208/jscej.23-16097>
- Tozawa, T., Yamazaki, D., & Oki, T. (2019). Development of global terrestrial model considering saturated lateral flow.
- von Humboldt, A. (1807). *Essay on the geography of plants (English translation 2009)*. The University of Chicago Press.
- Wood, E. F., Roundy, J. K., Troy, T. J., Van Beek, L. P. H., Bierkens, M. F. P., Blyth, E., et al. (2011). Hyperresolution global land surface modeling: Meeting a grand challenge for monitoring Earth's terrestrial water. *Water Resources Research*, 47(5), W05301. <https://doi.org/10.1029/2010wr010090>
- Yamazaki, D., de Almeida, G. A. M., & Bates, P. D. (2013). Improving computational efficiency in global river models by implementing the local inertial flow equation and a vector-based river network map. *Water Resources Research*, 49(11), 7221–7235. <https://doi.org/10.1002/wrcr.20552>
- Yamazaki, D., Ikeshima, D., Sosa, J., Bates, P. D., Allen, G. H., & Pavelsky, T. M. (2019). MERIT hydro: A high-resolution global hydrography map based on latest topography dataset. *Water Resources Research*, 55(6), 5053–5073. <https://doi.org/10.1029/2019WR024873>
- Yamazaki, D., Ikeshima, D., Tawatari, R., Yamaguchi, T., O'Loughlin, F., Neal, J. C., et al. (2017). A high-accuracy map of global terrain elevations. *Geophysical Research Letters*, 44(11), 5844–5853. <https://doi.org/10.1002/2017GL072874>
- Yamazaki, D., Kanae, S., Kim, H., & Oki, T. (2011). A physically based description of floodplain inundation dynamics in a global river routing model. *Water Resources Research*, 47(4), W04501. <https://doi.org/10.1029/2010WR009726>
- Yamazaki, D., Oki, T., & Kanae, S. (2009). Deriving a global river network map and its sub-grid topographic characteristics from a fine-resolution flow direction map. *Hydrology and Earth System Sciences*, 13(11), 2241–2251. <https://doi.org/10.5194/hess-13-2241-2009>
- Yan, J., Tong, M., Liu, J., Li, J., & Li, H. (2024). Temperature and moisture sensitivities of soil respiration vary along elevation gradients: An analysis from long-term field observations. *Science of the Total Environment*, 912, 169150. <https://doi.org/10.1016/j.scitotenv.2023.169150>

References From the Supporting Information

- Li, S., & Sawada, Y. (2022). Soil moisture-vegetation interaction from near-global in-situ soil moisture measurements. *Environmental Research Letters*, 17(11), 114028. <https://doi.org/10.1088/1748-9326/ac9c1f>
- Yang, Z., Dickinson, R. E., Henderson-Sellers, A., & Pitman, A. J. (1995). Preliminary study of spin-up processes in land surface models with the first stage data of project for intercomparison of land surface parameterization schemes phase 1 (a). *Journal of Geophysical Research*, 100(D8), 16553–16578. <https://doi.org/10.1029/95jd01076>